arXiv:1605.09191v1 [astro-ph.CO] 30 May 2016

Constraining light gravitino mass with 21 cm line observation

Yoshihiko Oyama [1] and Masahiro Kawasaki [1]

[1] *Institute for Cosmic Ray Research, The University of Tokyo, 5-1-5 Kashiwanoha, Kashiwa, Chiba 277-8582, Japan*

Abstract

We investigate how well we can constrain the mass of light gravitino $m_{3/2}$ by using future observations of 21 cm line fluctuations such as Square Kilometre Array (SKA) and Omniscope. Models with light gravitino with the mass $m_{3/2} \lesssim \mathcal{O}(10)$ eV are quite interesting because they are free from the cosmological gravitino problem and consistent with many baryogenesis/leptogenesis scenarios. We evaluate expected constraints on the mass of light gravitino from the observations of 21 cm line, and show that the observations are quite useful to prove the mass. If the gravitino mass is $m_{3/2} = 1$ eV, we found expected 1 σ errors on $m_{3/2}$ are $\sigma(m_{3/2}) = 0.25$ eV (SKA phase 1), 0.16 eV (SKA phase 2) and 0.067 eV (Omniscope) in combination with Planck + Simons Array + DESI (BAO) + H_0. Additionally, we also discuss detectability of the effective number of neutrino species by varying the effective number of neutrino species for light gravitino $N_{3/2}$ and constraints on the mass of light gravitino in the presence of massive neutrinos. We show that 21 cm line observations can detect the nonzero value of $N_{3/2}$, and allow us to distinguish the effects of the light gravitino from those of massive neutrino.

1 Introduction

In particle physics models with local super symmetry (SUSY) or supergravity, one of the most important predictions is the existing of gravitino, which is the superpartner of graviton and has a spin 3/2. The gravitino mass $m_{3/2}$ is related to the energy scales of SUSY breaking, and can vary from an order of eV up to of TeV. In particular, scenarios with light gravitino whose mass is $m_{3/2} \lesssim \mathcal{O}(10)$ eV are very interesting because they are free from the cosmological gravitino problem [1], and can be consistent with some baryogenesis scenarios which require a high reheating temperature such as thermal leptogenesis [2]. Therefore, the scenarios with the light gravitino are very attractive in cosmology.

It is important to determine the gravitino mass in order to understand the mechanism of SUSY breaking. Although it can be probed by collider experiments (e.g. LHC) [3] with direct and indirect signatures, we can also obtain constraints on it from cosmological observations [4]. In the early Universe, light gravitinos are produced from thermal plasma, and they behave as warm dark matter (WDM) at late epochs. The light gravitinos influence the growth of density fluctuations mainly through the following two effects. First of all, they change the time of matter-radiation equality because the light gravitinos behave as a radiation component at early epochs. Secondly, the light gravitinos have large velocity dispersions and propagate up to the horizon scales until they become non-relativistic.Then, they erase their own density fluctuation and suppress the growth of density fluctuations of matter below the free-streaming scale. However, the former effect is very small because the energy density of light gravitinos does not have a large fraction of the total energy of radiation. Therefore, we can probe signatures of the light gravitino mainly through the latter effect. From Lyman-α forest data in combination with WMAP [5], a constraint on the light gravitino mass is obtained, and its bound is $m_{3/2} < 16$ eV (95% C.L.). Additionally, some authors have pointed out that measurements of CMB lensing [6] or weak lensing surveys of galaxies [7] are quite effective in constraining the light gravitino mass. By using the date of CMB lensing from Planck and cosmic shear from the CHFTLenS survey, a stringent constraint is obtained, and the upper bound is $m_{3/2} < 4.7$ eV (95% C.L.) [8]. However, it is difficult to obtain significant bounds of the light gravitino mass if we treat the effective number of neutrino species for light gravitino $N_{3/2} \equiv \rho_{3/2}/\rho_\nu$ as a free parameter, where $\rho_{3/2}$ and ρ_ν are the energy densities of light relativistic gravitinos and neutrinos, respectively. Moreover, discriminating signatures of light gravitino from that of massive neutrino is also quite difficult. Therefore, if one wants to discriminate light gravitinos from other possibilities, it is mandatory to find a new powerful probe of cosmological signatures of the light gravitino.

In this paper, we particularly investigate the issue of how accurately we can constrain the light gravitino mass by using future observations of fluctuations of neutral hydrogen 21 cm line which comes from the epoch of reionization (EoR), in addition to those of CMB. By observing the power spectrum of cosmological 21 cm line fluctuations, we will be able to obtain useful information on a variety of cosmological parameters [9–18]. Because observations of the 21 cm line can cover a wide redshift range, they can be complementary

to other observations such as CMB. Additionally, the effects of the light gravitino mainly appear on small scales, which can be well measured by 21 cm observations. In order to discuss expected constraints from the future cosmological surveys on the mass of light gravitino, we make Fisher analysis by assuming the specifications for planned observations of 21 cm line such as Square Kilometre Array (SKA) [19] and Omniscope [20, 21]. In our analysis, we also take into account future CMB observations such as the Simons Array [22] and COrE+ [23]. Besides, we consider including information of a baryon acoustic oscillation (BAO) observation, such as Dark Energy Spectroscopic Instrument (DESI) [24] and a direct measurement of the Hubble constant H_0.

This paper is organized as follows. In Section 2, we briefly review the effects of light gravitino on cosmology. In Section 3, we review analytical methods used in this paper, paying particular attention to 21 cm line, CMB, BAO observations and the direct measurement of H_0. We show our results in Section 4, and Section 5 is devoted to our conclusion.

2 Light gravitino and its effects on large-scale structure in the Universe

2.1 Light gravitino

The existence of light gravitino is typically predicted in gauge-mediated SUSY breaking (GMSB) scenarios [25–30]. SUSY breaking is the origin of the masses of the gravitino and SUSY particles. The SUSY breaking field S has a vacuum expectation value as $\langle S \rangle = M + F_S \theta^2$, and F_S gives SUSY breaking scale, which is related to the gravitino mass $m_{3/2}$. The gravitino mass is given by

$$m_{3/2} = \frac{F_S}{\sqrt{3} M_{\rm pl}}, \tag{1}$$

where $M_{\rm pl} \simeq 2.4 \times 10^{18}$ GeV is the reduced Planck mass. On the other hand, in GMSB scenarios, sparticles in the standard model (SM) sector acquire their masses through messenger fields, whose mass scale is denoted as $M_{\rm mess}$. For example, in a GMSB model with N pairs of messenger particles, gaugino masses M_a ($a = 1, 2, 3$ is a gauge group index) and sfermion masses squared $m^2_{\tilde{f}_i}$ (i is a flavor index) are typically given by

$$M_a = N \left(\frac{\alpha_a}{4\pi} \right) \frac{F_S}{M_{\rm mess}}, \tag{2}$$

$$m^2_{\tilde{f}_i} = 2N \sum_a C_a^{(i)} \left(\frac{\alpha_a}{4\pi} \right)^2 \left(\frac{F_S}{M_{\rm mess}} \right)^2, \tag{3}$$

where $C_a^{(i)}$ is Casimir operators for the sfermion $\tilde{f}_i$, and α_a denotes the gauge coupling constants. Although $(F_S/M_{\rm mess}) \sim 100$ TeV is required in order to obtain TeV scale

masses, still the SUSY breaking scale F_S or the gravitino mass $m_{3/2}$ can take a wide range of values as $\mathcal{O}(1)\text{eV} \lesssim m_{3/2} \lesssim \mathcal{O}(10)\text{GeV}$, where the upper bound comes from the requirement that the gravity-mediation does not dominate, and existence of the lower bound arises from avoiding destabilization of the messenger scalar and not leading to unwanted vacua.

In the GMSB models, stringent constraints on the gravitino mass are obtained from the Higgs mass measured by LHC [31, 32]. In the minimal supersymmetric standard model (MSSM), the stop mass is required to be as large as $\mathcal{O}(10-100)$ TeV in order to achieve the measured large Higgs mass $m_h = 125$ GeV, and the bound can place a lower bound on the gravitino mass. In a class of GMSB models with N copies of messenger fields in the $5 + \bar{5}$ representation of SU(5), we can obtain a bound 300 eV $< m_{3/2}$ with $N = 1$, and 60 eV $< m_{3/2}$ with $N = 5$ [33], if the coupling between the messengers and the SUSY breaking field is perturbative. Although a range of the light gravitino mass which is allowed by present cosmological observations are ruled out, the bound by the LHC is model-dependent. For example, $\mathcal{O}(1-10)$ eV may be possible if the coupling is non-perturbative or a singlet Higgs is introduced (next to MSSM) [34].

Additionally, less stringent lower bounds are obtained from direct SUSY searches in LHC [35]. Assuming a perturbative coupling, we can obtain a lower bound 3.7eV $< m_{3/2}$ in the same GMSB model as mentioned above with $M_{\text{mess}} = 250$ TeV and $N = 3$ ($10 + \bar{10}$ of SU(5)).

2.2 Effects of light gravitino on the growth of density fluctuations

If we take account of the presence of the light gravitino in the early Universe, some difficulties arise in constructing a consistent cosmological scenarios, which we are going to describe shortly below. At the reheating era, gravitinos are efficiently produced and the abundance of them can easily exceed that of the present dark matter unless the reheating temperature T_R is very low [1]. However, many known baryogenesis/leptogenesis scenarios require high enough reheating temperature, which may be inconsistent with the upper bound coming from the observed abundance of dark matter. For example, thermal leptogenesis scenario [2] requires $T_{\text{R}} \gtrsim 10^9$ GeV and the reheating temperature seems to conflict with the gravitino problem except for the very light gravitino mass range $m_{3/2} \lesssim 100$ eV. If gravitinos have such a small mass, they are thermalized in the early Universe [4, 6]. In that case, their abundance does not have dependency on the reheating temperature and is smaller than the dark matter density if $m_{3/2} \lesssim 100$ eV. This advantage is the reason why we particularly focus on the light gravitino scenario.

Thermally produced gravitinos decouple from the other particles at some point, and their relic abundance is fixed. The number density is determined by the effective degrees of freedom $g_{*3/2}$ at the decoupling of the gravitinos. In [4, 6], the number density of the gravitinos in GMSB models is evaluated by solving the Boltzmann equation, and for a messenger mass scale $M_{\text{mess}} \sim 100$ TeV, $g_{*3/2}$ becomes $g_{*3/2} \sim 90$ [6] with only mild

dependence on $m_{3/2}$. In consideration of the result, we set $g_{*3/2} = 90$ as the fiducial value in our analysis.

The thermally produced light gravitinos behave as a warm dark matter component [4, 6], and they can be parametrized by their temperature and mass. Since gravitinos interact with other particles through their goldstino components in the GMSB scenario, their phase-space distribution is a Fermi-Dirac distribution with two degrees of freedom. Because light gravitinos behave as relativistic particles at early epoch, we can parametrize its energy density $\rho_{3/2}$ by using the effective number of neutrino species, and it is given by

$$N_{3/2} = \frac{\rho_{3/2}}{\rho_\nu} = \left(\frac{T_{3/2}}{T_\nu}\right)^4 = \left(\frac{g_{*\nu}}{g_{*3/2}}\right)^{4/3}, \tag{4}$$

where ρ_ν is the energy density of one generation of neutrinos , and $g_{*3/2}$ and $g_{*\nu}$ are the effective degrees of freedom at decoupling of light gravitinos and neutrinos, respectively. In standard cosmology, the degree of freedom of neutrinos at the neutrino decoupling is $g_{*\nu} = 10.75$. $T_{3/2}$ and T_ν are temperatures of light gravitinos and neutrinos, respectively. From Eq. (4), the temperature of light gravitino at present is evaluated as

$$T_{3/2} = \left(N_{3/2}\right)^{1/4} T_\nu = 1.95 \left(N_{3/2}\right)^{1/4} \mathrm{K}, \tag{5}$$

where we use the temperature of neutrinos in the standard cosmology.

At late epochs, light gravitinos lose their energy and become non-relativistic particles due to the cosmic expansion. Its present density parameter $\Omega_{3/2}h^2$ can be estimated as

$$\Omega_{3/2}h^2 = 0.1269 \left(\frac{m_{3/2}}{100\ \mathrm{eV}}\right) \left(\frac{90}{g_{*3/2}}\right). \tag{6}$$

In the following, we assume that dark matter does not consists solely of the light gravitinos because the gravitino mass $m_{3/2}$ needs to be about 90 eV in order to be consistent with observed dark matter density $\Omega_{\mathrm{DM}} \simeq 0.11$ [36], which contradicts with the constraint from Ly-α forest, $m_{3/2} < 16$ eV [5], as well as a more recent one $m_{3/2} < 4.7$ eV from CMB and cosmic shear data [8]. Therefore, we assume that dark matter consists of the light gravitino and CDM components. i.e. $\Omega_{\mathrm{DM}} = \Omega_{\mathrm{CDM}} + \Omega_{3/2}$, and we define the fraction of gravitino in the total dark matter density as

$$f_{3/2} \equiv \frac{\Omega_{3/2}}{\Omega_{\mathrm{DM}}}. \tag{7}$$

As the CDM component, the QCD axion, a messenger baryon proposed in [37] and so on can be well-fitted within the framework of the GMSB scenario.

From now on, we briefly explain effects of the light gravitinos on cosmological structure formation. They behave as a warm dark matter component, and their effects on structure formation can be understood by considering the following two aspects: (i) a contribution to the energy density of radiation (ii) suppression of matter fluctuations on small scales

through the free-streaming. The first effect is due to the fact that light gravitinos behave as relativistic particles at early epochs. Therefore, the time of matter-radiation equality is slightly delayed if light gravitinos exist in the Universe. The delay alters the evolution of gravitational potential and drives the integrated Sachs-Wolfe (ISW) effect in the CMB temperature anisotropy. In addition, the matter fluctuations are suppressed at small scales through stagspansion effect due to the delaying of matter-radiation equality. However, its contribution is so small (as we mentioned before, the theoretical calculation predicts that $g_{*3/2}$ is around 90, which corresponds to $N_{3/2} \simeq 0.059$ [6]), and it is difficult to measure the impacts due to this effect by observing CMB anisotropies without lensing. Therefore, constraints on the gravitino mass mainly come from the second effect, i.e. its free-streaming behavior. Because light gravitinos have relatively large thermal velocity, they propagate up to their free-streaming scale and erase own density fluctuation in a similar manner to massive neutrinos. Within the free-streaming scale, light gravitinos do not contribute to the gravitational growth of the matter fluctuations. Thus, matter fluctuations at small scales are suppressed in comparison to the ΛCDM model.

Massive neutrinos also have similar effects on the growth of matter fluctuations, but its temperature and energy density are different from those of light gravitinos. Therefore, in principle, we can discriminate between the effects of the light gravitino and the massive neutrino through observing their free streaming scale.

3 Forecasting methods

3.1 21 cm line

Here, we briefly review a forecasting method related to 21 cm line observations in our analysis. For further details of the 21 cm line observations, we refer to Refs. [38, 39].

3.1.1 Power spectrum of 21 cm radiation

The 21 cm line of neutral hydrogen atom is emitted by transition between the hyperfine splitting of the 1s ground state. We can observe signals of 21 cm line which come from the epoch of reionization (EoR) or the cosmic dark ages as the differential brightness temperature relative to the temperature of CMB $T_{\rm CMB}$:

$$\Delta T_b(\boldsymbol{r}, z) = \frac{3c^3 h A_{21}}{32\pi k_B \nu_{21}^2} \frac{x_{HI}(\boldsymbol{r}, z) n_H(\boldsymbol{r}, z)}{(1+z)H(z)} \left(1 - \frac{T_{\rm CMB}(\boldsymbol{r}, z)}{T_S(\boldsymbol{r}, z)}\right) \left(1 - \frac{1+z}{H(z)} \frac{dv_{p\parallel}(\boldsymbol{r}, z)}{dr_\parallel}\right), \tag{8}$$

where $\boldsymbol{r}$ is the comoving coordinates of the source of 21 cm line, z represents the redshift at emission/absorption, $A_{21} \simeq 2.869 \times 10^{-15}\mathrm{s}^{-1}$ is the spontaneous decay rate of the hyperfine splitting, $\nu_{21} \simeq 1.42$ GHz is the frequency of 21 cm line, n_H is the number density of hydrogen, x_{HI} is the fraction of neutral hydrogen, and $dv_{p\parallel}/dr_\parallel$ is the gradient of peculiar velocity along the line of sight. T_S is the spin temperature, which is defined by

$n_1/n_0 = 3\exp(-T_{21}/T_S)$, where n_0 and n_1 are the number densities of singlet and triplet states of neutral hydrogen atom, respectively. Here $T_{21} = hc/k_B\lambda_{21}$ is the temperature corresponding to 21 cm line, and λ_{21} is its wavelength.

In this paper, we assume that $T_S \gg T_{\rm CMB}$ because we focus on the epoch of reionization during which this condition is well satisfied. In general, the brightness temperature is sensitive to details of inter-galactic medium (IGM) and astrophysical processes. However, with a few reasonable assumptions, we can eliminate the dependence from the 21 cm line brightness temperature [40–42]. At the epoch of reionization long after star formation begins, X-ray background produced by early stellar remnants heats the IGM. Therefore, kinetic temperature of the IGM T_K becomes much higher than that of CMB $T_{\rm CMB}$. Furthermore, the star formation produces a large amount of Lyα photons sufficient to couple T_S to T_K through the Wouthuysen-Field effect [43,44]. In this scenario, $T_{\rm CMB} \ll T_K \sim T_S$ are justified at $z \lesssim 10$, and ΔT_b does not depend on T_S.

Now, let us consider fluctuations of the differential brightness temperature of 21 cm line $\Delta T_b(\boldsymbol{r})$. By expanding the hydrogen number density n_H and the ionization fraction x_i ($x_i = 1 - x_{HI}$) as $n_H(\boldsymbol{r}) = \bar{n}_H(1+\delta(\boldsymbol{r}))$ and $x_i(\boldsymbol{r}) = \bar{x}_i(1+\delta_x(\boldsymbol{r}))$, we can rewrite Eq. (8) as

$$\Delta T_b(\boldsymbol{r}, z) = \Delta\bar{T}_b(z)\left(1 - \bar{x}_i(1+\delta_x(\boldsymbol{r}, z))\right)\left(1+\delta(\boldsymbol{r}, z)\right)\left(1 - \frac{1+z}{H(z)}\frac{dv_{p\parallel}(\boldsymbol{r}, z)}{dr_\parallel}\right), \quad (9)$$

where we assume that $T_{\rm CMB} \ll T_S$ and neglect the term including the spin temperature. Here, $\Delta\bar{T}_b$ is the spatially averaged differential brightness temperature at redshift z and given by

$$\Delta\bar{T}_b(z) \simeq 26.8\left(\frac{1-Y_p}{1-0.25}\right)\left(\frac{\Omega_b h^2}{0.023}\right)\left(\frac{0.15}{\Omega_m h^2}\frac{1+z}{10}\right)^{1/2}\ {\rm mK}, \quad (10)$$

where Y_p is the primordial ^{4}He mass fraction. By denoting the fluctuation of ΔT_b as $\delta(\Delta T_b(\boldsymbol{r}, z)) \equiv \Delta T_b(\boldsymbol{r}, z) - \bar{x}_H(z)\Delta\bar{T}_b({\rm z})$, the 21 cm line power spectrum $P_{21}(\boldsymbol{k})$ in the k-space is defined by

$$\langle\delta(\Delta T_b^*(\boldsymbol{k}))\delta(\Delta T_b(\boldsymbol{k'}))\rangle = (2\pi)^3\delta^3(\boldsymbol{k}-\boldsymbol{k'})P_{21}(\boldsymbol{k}). \quad (11)$$

Because the Fourier component of the peculiar velocity term $\delta_v \equiv (1+z)(dv_{p\parallel}/dr_\parallel)/H(z)$ is given by $\delta_v(\boldsymbol{k}) = -\mu^2\delta(\boldsymbol{k})$ within the linear perturbation theory ($\mu = \hat{\boldsymbol{k}}\cdot\hat{\boldsymbol{n}}$ is the cosine of the angle between the wave vector and the line of sight), the power spectrum can be written as

$$P_{21}(\boldsymbol{k}) = P_{\mu^0}(k) + \mu^2 P_{\mu^2}(k) + \mu^4 P_{\mu^4}(k), \quad (12)$$

where $k = |\boldsymbol{k}|$ and

$$P_{\mu^0} = \mathcal{P}_{\delta\delta} - 2\mathcal{P}_{x\delta} + \mathcal{P}_{xx}, \quad (13)$$

$$P_{\mu^2} = 2\left(\mathcal{P}_{\delta\delta} - \mathcal{P}_{x\delta}\right), \quad (14)$$

$$P_{\mu^4} = \mathcal{P}_{\delta\delta}. \quad (15)$$

z	$\bar{x}_H$	b_{xx}^2	R_{xx} [Mpc]	α_{xx}	γ_{xx}	$b_{x\delta}^2$	$R_{x\delta}$ [Mpc]	$\alpha_{x\delta}$
9.2	0.9	0.208	1.24	-1.63	0.38	0.45	0.56	-0.4
8.0	0.7	2.12	1.63	-0.1	1.35	1.47	0.62	0.46
7.5	0.5	9.9	1.3	1.6	2.3	3.1	0.58	2.0
7.0	0.3	77.0	3.0	4.5	2.05	8.2	0.143	28.0

Table 1: Fiducial values of the parameters characterizing $\mathcal{P}_{xx}(k)$ and $\mathcal{P}_{x\delta}(k)$ (See Eqs. (16) and (17)) [45].

Here, $\mathcal{P}_{\delta\delta} \equiv (\Delta\bar{T}_b)^2\bar{x}_{HI}^2 P_{\delta\delta}, \mathcal{P}_{x\delta} \equiv (\Delta\bar{T}_b)^2\bar{x}_i\bar{x}_{HI}P_{x\delta}$ and $\mathcal{P}_{xx} \equiv (\Delta\bar{T}_b)^2\bar{x}_i^2 P_{xx}$, where $P_{\delta\delta}, P_{x\delta}$ and P_{xx} are the auto- and cross- power spectra defined in the same manner as Eq. (11) for the fluctuation of hydrogen number density δ and that of ionization fraction δ_x. Since $P_{\delta\delta}$ traces the fluctuation of matter, the power spectrum of 21 cm line has information on cosmological parameters.

$P_{x\delta}$ and P_{xx} can be neglected as long as we consider eras when the IGM is completely neutral. However, after the reionization starts, these two spectra significantly contribute to the 21 cm line power spectrum. In order to evaluate these spectra, we adopt the treatment given in Ref. [45], where they assumed that $\mathcal{P}_{x\delta}$ and $\mathcal{P}_{xx}$ have specific forms which match simulations incorporating radiative transfer in Refs. [46, 47]. The explicit forms of the power spectra are parametrized to be

$$\mathcal{P}_{xx}(k) = b_{xx}^2 \left[1 + \alpha_{xx}(kR_{xx}) + (kR_{xx})^2\right]^{-\gamma_{xx}/2} \mathcal{P}_{\delta\delta}(k), \tag{16}$$

$$\mathcal{P}_{x\delta}(k) = b_{x\delta}^2 \; e^{-\alpha_{x\delta}(kR_{x\delta}) - (kR_{x\delta})^2} \mathcal{P}_{\delta\delta}(k), \tag{17}$$

where b_{xx}, $b_{x\delta}$, α_{xx}, γ_{xx} and $\alpha_{x\delta}$ are parameters which characterize the amplitudes and the shapes of these spectra, and R_{xx} and $R_{x\delta}$ represent the effective size of ionized bubbles. In our analysis, we adopt the values listed in Table 1 as the fiducial values of these parameters.

We note that the power spectrum in the k-space $P_{21}(\boldsymbol{k})$ are not directly measured by 21 cm line observations. Instead, the angular location on the sky and the frequency are measured by an experiment, and they can be specified by the following vector

$$\boldsymbol{\Theta} = \theta_x\hat{e}_x + \theta_y\hat{e}_y + \Delta f\hat{e}_z \equiv \boldsymbol{\Theta}_\perp + \Delta f\hat{e}_z, \tag{18}$$

where Δf represents the frequency difference from the central redshift z of a given redshift bin. Then, we can define the Fourier dual of $\boldsymbol{\Theta}$ as

$$\boldsymbol{u} \equiv u_x\hat{e}_x + u_y\hat{e}_y + u_\parallel\hat{e}_z \equiv \boldsymbol{u}_\perp + u_\parallel\hat{e}_z. \tag{19}$$

Notice that $u_\parallel$ has the unit of time since it is the Fourier dual of Δf. With the flat-sky approximation[1], we can linearize the relations between $\boldsymbol{r}$ and $\boldsymbol{\Theta}$, and they are given by

$$\boldsymbol{\Theta}_\perp = \boldsymbol{r}_\perp/d_A(z), \qquad \Delta f = \Delta r_\parallel/y(z), \tag{20}$$

[1] Even if we consider all-sky experiments, the flat-sky approximation can be valid as long as we analyze the data in a lot of small patches of the sky [45].

where $\boldsymbol{r}_\perp$ is the vector perpendicular to the line of sight, $\Delta r_\parallel$ is the comoving distance interval corresponding to the frequency intervals Δf, $d_A(z)$ is the comoving angular diameter distance, and $y(z) \equiv \lambda_{21}(1+z)^2/H(z)$. Then, the relations between $\boldsymbol{k}$ and $\boldsymbol{u}$ can be written as

$$\boldsymbol{u}_\perp = d_A \boldsymbol{k}_\perp, \qquad u_\parallel = y k_\parallel. \tag{21}$$

The power spectrum of ΔT_b in the u-space can be defined in the same manner as the treatment in the k-space, and the spectra are related each other by

$$P_{21}(\boldsymbol{u}) = \frac{1}{d_A(z)^2 y(z)} P_{21}(\boldsymbol{k}). \tag{22}$$

We use the u-space power spectrum in the following analysis because this quantity is directly measurable without assuming cosmological parameters.

3.1.2 Fisher matrix of 21 cm line observation

In order to estimate errors of cosmological parameters, we use the Fisher matrix analysis [48]. The Fisher matrix of 21 cm line observations is given by [9]

$$F_{\alpha\beta}^{(21\mathrm{cm})} = \sum_{\mathrm{pixels}} \frac{1}{[\delta P_{21}(\boldsymbol{u})]^2} \left(\frac{\partial P_{21}(\boldsymbol{u})}{\partial \theta_\alpha} \right) \left(\frac{\partial P_{21}(\boldsymbol{u})}{\partial \theta_\beta} \right), \tag{23}$$

where $\delta P_{21}(\boldsymbol{u})$ is the error in the power spectrum measurements for a Fourier pixel $\boldsymbol{u}$, and θ_α represents a cosmological parameter with its index "α". The 1 σ error of the parameter θ_α is evaluated by the Fisher matrix, and we can obtain the estimated error from

$$\Delta\theta_\alpha \geq \sqrt{(F^{-1})_{\alpha\alpha}}. \tag{24}$$

When we differentiate $P_{21}(\boldsymbol{u})$ with respect to the cosmological parameters, we fix $\mathcal{P}_{\delta\delta}(k)$ in Eqs. (16) and (17) so that we get conservative evaluations for errors of cosmological parameters. Then, the information of the matter distribution only comes from the $\mathcal{P}_{\delta\delta}(k)$ terms in P_{μ^0}, P_{μ^2} and P_{μ^4}.

The error of the power spectrum $\delta P_{21}(\boldsymbol{u})$ consists of sample variances and experimental noises

$$\delta P_{21}(\boldsymbol{u}) = \frac{P_{21}(\boldsymbol{u}) + P_N(u_\perp)}{N_c^{1/2}}, \tag{25}$$

where the first term on the right hand side represents the sample variance, and the second term gives contribution of experimental noises. Here, $N_c = 2\pi k_\perp \Delta k_\perp \Delta k_\parallel V(z)/(2\pi)^3$ is the number of independent cells in an annulus summing over the azimuthal angle, $V(z) = d_A(z)^2 y(z) B \times \mathrm{FoV}$ is the survey volume, where B is the bandwidth, and FoV $\propto \lambda^2$ is the field of view of an interferometer.

	$N_{\rm ant}$	A_e $(z=8)$ [m^2]	$L_{\rm min}$ [m]	$L_{\rm max}$ [km]	FoV $(z=8)$ [deg^2]	Obs. time t_0 [hour]	z
SKA phase 1	911/2	443	35	6	13.12	1000	6.8 – 10
SKA phase 2	911× 4	443	35	6	13.12 × 4 × 4	1000	6.8 – 10
Omniscope	10^6	1	1	1	2.063 $\times 10^4$	1000	6.8 – 10

Table 2: Specifications of 21 cm observations adopted in the analysis.

3.1.3 Specifications of experiments

Here, we show the specifications of the 21 cm line observations which is considered in this paper.

Survey range: In our analyses, we assume that the redshift range used for constraining cosmological parameters is $z = 6.75 - 10.05$, which we divide into 4 bins: $z = 6.75 - 7.25, 7.25 - 7.75, 7.75 - 8.25$ and $8.25 - 10.05$. For surveyed scales (wave number), we set a minimum cut off $k_{\rm min\parallel} = 2\pi/(yB)$ in order to avoid foreground contaminations [9], and take a maximum value $k_{\rm max} = 2$ Mpc^{-1} in order not to be affected by nonlinear effects of matter fluctuations, which becomes important on $k_{\rm max} \leq k$.

For methods of foreground removals, see also recent discussions about the independent component analysis (ICA) algorithm (FastICA) [49], which will be developed in terms of the ongoing LOFAR observation [50].

Noise power spectrum: The noise power spectrum, $P_N(u_\perp)$ appeared in Eq. (25) is given by

$$P_N(u_\perp) = \left(\frac{\lambda^2(z) T_{\rm sys}(z)}{A_e(z)}\right)^2 \frac{1}{t_0 n(u_\perp)}, \tag{26}$$

where λ is an observed wave length of redshifted 21 cm line, A_e is the effective collecting area per a antenna tile or a station, t_0 is the observation time, $n(u_\perp)$ is the number density of baseline, and the system temperature $T_{\rm sys}$ is estimated to be $T_{\rm sys} = T_{\rm sky} + T_{\rm rcvr}$ and is dominated by the sky temperature due to synchrotron radiation. Here, $T_{\rm sky} = 60(\lambda/[m])^{2.55}$ [K] is the sky temperature, and $T_{\rm rcvr} = 0.1 T_{\rm sky} + 40$[K] is the receiver noise [19]. The effective collecting area is proportional to the square of the observed wave length $A_e \propto \lambda^2$. The number density of the baseline $n(u_\perp)$ depends on an antenna distribution.

As future observations of 21cm line fluctuations, in this paper we consider SKA (phase 1 and phase 2) [19, 51] and Omniscope [20, 21], whose specifications are shown in Table 2. In order to estimate the number density of the baseline $n(u_\perp)$, we assume a realization of antenna distributions for these arrays as follows. The total collecting area of SKA phase 1 (SKA1) is one-half as large as that of the originally planned SKA1. Therefore, for SKA1, we assume that the number of antenna station $N_{\rm ant}$ is half as many as that of the originally

planned SKA1, which has 911 antenna stations, and for SKA phase 2 (SKA2), the number of antenna stations is 4 times as many as that of the originally planned SKA1.

The number density of baselines of the originally planned SKA1 is determined as follows. We take the antenna stations in a core region with a radius 3000 m, which consists of 95% of the total. and the distribution has an antenna station density profile of the originally planned SKA1 $\rho_{\rm origSKA1}(r)$ (r: a radius from center of the array) as follows [15],

$$\rho_{\rm origSKA1}(r) = \begin{cases} \rho_0 r^{-1}, & \rho_0 \equiv \frac{13}{16\pi\left(\sqrt{10}-1\right)}\ {\rm m}^{-2} & r \leq 400\ {\rm m}, \\ \rho_1 r^{-3/2}, & \rho_1 \equiv \rho_0 \times 400^{1/2}, & 400\ {\rm m} < r \leq 1000\ {\rm m}, \\ \rho_2 r^{-7/2}, & \rho_2 \equiv \rho_1 \times 1000^2, & 1000\ {\rm m} < r \leq 1500\ {\rm m}, \\ \rho_3 r^{-9/2}, & \rho_3 \equiv \rho_2 \times 1500, & 1500\ {\rm m} < r \leq 2000\ {\rm m}, \\ \rho_4 r^{-17/2}, & \rho_4 \equiv \rho_3 \times 2000^4, & 2000\ {\rm m} < r \leq 3000\ {\rm m}. \end{cases} \tag{27}$$

Here, we assume an azimuthally symmetric distribution of the antenna stations in SKA. In this analysis, we ignore measurements from the sparse distribution of the remaining 5% of the total antenna stations which are outside the core region. This distribution agrees with the specification of the originally planned SKA1 baseline design.

Then we can evaluate the number density of baselines of the originally planned SKA1 $n_{\rm origSKA1}(u_\perp)$ from this distribution. Using the number density of baselines, we can estimate that the number densities of baselines of SKA1 (re-baseline design) and SKA2 are

$$n_{\rm SKA1}(u_\perp) = n_{\rm origSKA1}(u_\perp) \times \left(\frac{1}{2}\right)^2, \tag{28}$$

$$n_{\rm SKA2}(u_\perp) = n_{\rm origSKA1}(u_\perp) \times 4^2, \tag{29}$$

where $n_{\rm SKA1}(u_\perp)$ and $n_{\rm SKA2}(u_\perp)$ are the number densities of baseline of SKA1 or SKA2, respectively.

For Omniscope, which is a future square-kilometre collecting area array optimized for 21 cm tomography, we take all of antenna tiles distributed with a filled nucleus in the same manner as Ref. [45].

3.2 CMB

In our analysis, we focus on not only 21cm line observations but also CMB observations, especially gravitational lensing of CMB, which has information on matter fluctuations at late times. Although the 21 cm line observations are powerful probes of the matter power spectrum, particularly, on small scales, the CMB observations greatly help to determine other cosmological parameters such as energy densities of the dark matter, baryons and the dark energy.

Besides, CMB power spectra are sensitive to gravitino mass through the CMB lensing. Future precise CMB experiments are expected to set stringent constraints on the light

gravitino mass [6]. Therefore, we take account of combining the CMB experiments with the 21 cm line observations.

3.2.1 Fisher matrix of CMB

We evaluate errors of cosmological parameters by using the Fisher matrix of CMB, which is given by [48]

$$F_{\alpha\beta}^{(\mathrm{CMB})} = \sum_{\ell} \frac{(2\ell+1)}{2} \mathrm{Tr}\left[C_\ell^{-1} \frac{\partial C_\ell}{\partial \theta_\alpha} C_\ell^{-1} \frac{\partial C_\ell}{\partial \theta_\beta} \right], \tag{30}$$

$$C_\ell = \begin{pmatrix} C_\ell^{\mathrm{TT}} + N_\ell^{\mathrm{TT}} & C_\ell^{\mathrm{TE}} & C_\ell^{\mathrm{Td}} \\ C_\ell^{\mathrm{TE}} & C_\ell^{\mathrm{EE}} + N_\ell^{\mathrm{EE}} & 0 \\ C_\ell^{\mathrm{Td}} & 0 & C_\ell^{\mathrm{dd}} + N_\ell^{\mathrm{dd}} \end{pmatrix}, \tag{31}$$

where ℓ is the multipole of angular power spectra, $C_\ell^{\mathrm{X}}\,(\mathrm{X} = \mathrm{TT}, \mathrm{EE}, \mathrm{TE})$ are the CMB power spectra, C_ℓ^{dd} is the deflection angle spectrum, C_ℓ^{Td} is the cross correlation between the deflection angle and the temperature, $N_\ell^{\mathrm{X}'}\,(\mathrm{X}' = \mathrm{TT}, \mathrm{EE})$ and N_ℓ^{dd} are the noise power spectra, where C_ℓ^{dd} is calculated by a lensing potential [59] and is related with the lensed CMB power spectra. The noise power spectra of CMB $N_\ell^{\mathrm{X}'}$ are expressed with a beam size $\sigma_{\mathrm{beam}}(\nu) = \theta_{\mathrm{FWHM}}(\nu)/\sqrt{8\ln 2}$, where $\sqrt{8\ln 2}\sigma_{\mathrm{beam}}$ means the full width at half maximum of the Gaussian distribution, and instrumental sensitivity $\Delta_{\mathrm{X}'}(\nu)$ by

$$N_\ell^{\mathrm{X}'} = \left[\sum_i \frac{1}{n_\ell^{\mathrm{X}'}(\nu_i)} \right]^{-1}, \tag{32}$$

where ν_i is an observing frequency and

$$n_\ell^{\mathrm{X}'}(\nu) = \Delta_{\mathrm{X}'}^2(\nu) \exp\left[\ell(\ell+1)\sigma_{\mathrm{beam}}^2(\nu) \right]. \tag{33}$$

The noise power spectrum of deflection angle N_l^{dd} is obtained assuming lensing reconstruction with the quadratic estimator [59], which is computed with FUTURCMB [60]. In this algorithm, N_ℓ^{dd} is estimated from the noise $N_\ell^{X'}$, and lensed and unlensed power spectra of CMB temperature, E-mode and B-mode polarizations.

Finally, the Fisher matrix in Eq.(30) is modified as follows by taking into account the multipole range $[\ell_{min}, \ell_{max}]$ and the fraction of the observed sky f_{sky},

$$F_{\alpha\beta}^{(\mathrm{CMB})} = \sum_{\ell=\ell_{min}}^{\ell_{max}} \frac{(2\ell+1)}{2} f_{\mathrm{sky}} \mathrm{Tr}\left[C_\ell^{-1} \frac{\partial C_\ell}{\partial \theta_\alpha} C_\ell^{-1} \frac{\partial C_\ell}{\partial \theta_\beta} \right]. \tag{34}$$

3.2.2 Specifications of the experiments

Now, we show the specifications of the CMB observations which are considered in this paper. In order to obtain the future constraints, we consider Planck [67], the Simons Array [22], which we occasionally abbreviate to SA in this paper, and COrE+ [23] whose experimental specifications are summarized in Tables 3 and 4. The Simons Array is a near future ground-based precise CMB polarization observation and COrE+ is a planned satellite observing CMB.

When we combine observations of Planck and the Simons Array, we evaluate the noise power spectra $N_\ell^{\rm X,Planck+SA}$ of the CMB polarization (X = EE or BB) with the following operation:

(1) $2 \leq \ell < 25$

$$N_\ell^{\rm X,Planck+SA} = N_\ell^{\rm X,Planck}, \tag{35}$$

(2) $25 \leq \ell \leq 3000$

$$N_\ell^{\rm X,Planck+SA} = [1/N_\ell^{\rm X,Planck} + 1/N_\ell^{\rm X,SA}]^{-1}. \tag{36}$$

Since we assume that the CMB temperature fluctuation observed by the Simons Array is not used for constraints on the cosmological parameters, the temperature noise power spectrum $N_\ell^{\rm TT,\,Planck+SA}$ is equal to $N_\ell^{\rm TT,\,Planck}$. The reason for this is that the CMB temperature fluctuation observed by Planck reaches almost cosmic variance limit. Therefore, the constraints are not significantly improved if we include the CMB temperature fluctuation observed by the Simons Array.

3.3 BAO

In our analysis, we take account of joint constraints from CMB, 21cm line, baryon acoustic oscillation (BAO). Therefore, before discussing future constraints, we briefly summarize formalisms of our analysis methods related to BAO, here.

3.3.1 Fisher matrix of BAO

For estimating future constrains, we use the following Fisher matrix of BAO data. The following method is based on [68] and [69]. The observables of BAO are the comoving angular diameter distance $d_A(z)$ and the Hubble parameter $H(z)$ (and more specifically, $\ln(d_A(z))$ and $\ln(H(z))$ are the observables). Therefore, the Fisher matrix of BAO data is written as

$$F_{\alpha\beta}^{({\rm BAO})\ d,H} = \sum_i \frac{1}{\sigma_{d,H}^2(z_i)} \frac{\partial f_i^{d,H}}{\partial\theta_\alpha} \frac{\partial f_i^{d,H}}{\partial\theta_\beta}, \tag{37}$$

$$f_i^d = \ln(d_A(z_i)), \tag{38}$$

$$f_i^H = \ln(H(z_i)), \tag{39}$$

Experiment	ν [GHz]	$\Delta_{\rm TT}$ [μKarcmin]	$\Delta_{\rm PP}$ [μKarcmin]	$\theta_{\rm FWHM}$ [arcmin]	$f_{\rm sky}$	$\ell_{\rm min}$	$\ell_{\rm max}$
Planck	30	145	205	33	0.65	2	3000
	44	150	212	23			
	70	137	195	14			
	100	64.6	104	9.5			
	143	42.6	80.9	7.1			
	217	65.5	134	5			
	353	406	406	5			
Simons Array	95	-	13.9	5.2	0.65	25	3000
	150	-	11.4	3.5			
	220	-	38.8	2.7			

Table 3: Experimental specifications of Planck and the Simons Array assumed in our analysis [18]. Here ν is the observation frequency, $\Delta_{\rm TT}$ is the temperature sensitivity per $1' \times 1'$ pixel, $\Delta_{\rm PP} = \Delta_{\rm EE} = \Delta_{\rm BB}$ is the polarization (E-mode and B-mode) sensitivity per $1' \times 1'$ pixel, $\theta_{\rm FWHM}$ is the angular resolution defined to be the full width at half-maximum, and $f_{\rm sky}$ is the observed fraction of the sky. For the Planck experiment, we assume that the three frequency bands $(70, 100, 143$ GHz) are only used for the observation of CMB. For the Simons Array, we assume that the 95 and 150 GHz bands are used for observation of CMB, and the 220 GHz band is not used for constraining cosmological parameters because the band is found to be useful for the foreground removal [17, 18].

Experiment	ν [GHz]	$\Delta_{\rm TT}$ [μKarcmin]	$\Delta_{\rm PP}$ [μKarcmin]	$\theta_{\rm FWHM}$ [arcmin]	$f_{\rm sky}$	$\ell_{\rm min}$	$\ell_{\rm max}$
COrE+	45	5.2	9.0	23.3	0.65	2	3000
	75	2.7	4.7	14			
	105	2.7	4.6	10			
	135	2.6	4.5	7.7			
	165	2.6	4.6	6.4			
	195	2.6	4.5	5.4			
	225	2.6	4.5	4.7			
	255	6.0	10.4	4.1			
	285	10.0	17	3.7			
	315	26.6	46	3.3			
	375	67.8	117	2.8			
	435	147.6	255	2.4			
	555	218	589	1.9			
	675	1268	3420	1.6			
	795	7744	20881	1.3			

Table 4: Experimental specifications of COrE+ adopted in our analysis. Because specifications of COrE+ are in the planning stage, we use the values appeared in Ref. [23], which are original specifications of COrE. In the same manner as Ref. [23], we assume that the CMB channels are 75, 105, 135, 165, 195 and 225 GHz.

Central redshift z_i	$\sigma_d(z_i) \times 10^2$	$\sigma_H(z_i) \times 10^2$
0.15	2.78	5.34
0.25	1.87	3.51
0.35	1.45	2.69
0.45	1.19	2.20
0.55	1.01	1.85
0.65	0.87	1.60
0.75	0.77	1.41
0.85	0.76	1.35
0.95	0.88	1.42
1.05	0.91	1.41
1.15	0.91	1.38
1.25	0.91	1.36
1.35	1.00	1.46
1.45	1.17	1.66
1.55	1.50	2.04
1.65	2.36	3.15
1.75	3.62	4.87
1.85	4.79	6.55

Table 5: Specification of DESI (14000 [deg^2]) adopted in the analysis. These values are the same as those in Ref. [70].

where i is the index of each redshift bin, $\sigma_d(z_i)$ and $\sigma_H(z_i)$ are variances of $\ln(d_A(z_i))$ and $\ln(H(z_i))$, respectively. We assume that an observed redshift range is divided into bins, with the width and central redshift value of each bin respectively denoted as Δz_i and z_i.

Note that cosmological parameters related to BAO data are only $(\Omega_m h^2, \Omega_\Lambda)$ or (h, Ω_Λ) when we assume that the Universe is flat.

3.3.2 Specifications of BAO data and the direct measurement of the Hubble constant

In this paper, we focus on the Dark Energy Spectroscopic Instrument (DESI) [24, 70], which is a future large volume galaxy survey. The survey redshift range is $0.1 < z < 1.9$ (we do not include the Ly-α forest at $1.9 < z$ for simplicity), where we assume that the redshift range is divided into 18 bins, in other words $\Delta z_i = 0.1$, and the observed solid angle is 14000 [deg^2]. We summarize the specifications of DESI in Table. 5 [70].

Additionally, in the same manner as [69], when we combine BAO with the other observations, we add a 1% H_0 prior, which would be achievable by a direct measurements of the Hubble constant in the next decade. The Fisher matrix of the direct measurement of

H_0 is expressed as

$$F_{\alpha\beta}^{(H_0)} = \begin{cases} \frac{1}{(1\% \times H_{0,\mathrm{fid}})^2}, & \theta_\alpha = \theta_\beta = H_0, \\ 0, & \text{the other components}, \end{cases} \tag{40}$$

where $H_{0,\mathrm{fid}}$ is the fiducial value of H_0. If we choose the Hubble parameter as a dependent parameter, it is necessary to translate the Fisher matrix into that of a chosen parameter space. Under the translation of $(h, \Omega_\Lambda) \longrightarrow (\Omega_m h^2, \Omega_\Lambda)$, the Fisher matrix in the new parameter space is written as

$$\tilde{F}^{H_0} = \begin{pmatrix} \tilde{F}_{\Omega_m h^2 \Omega_m h^2} & \tilde{F}_{\Omega_m h^2 \Omega_\Lambda} \\ \tilde{F}_{\Omega_m h^2 \Omega_\Lambda} & \tilde{F}_{\Omega_\Lambda \Omega_\Lambda} \end{pmatrix} = \frac{1}{(1\% \times H_{0,\mathrm{fid}})^2} \left(\frac{1}{2\Omega_m h^2} \right)^2 \begin{pmatrix} h^2 & h^4 \\ h^4 & h^6 \end{pmatrix}. \tag{41}$$

4 Results

In this section, we present our results for projected constraints by 21cm line (SKA phase 1, phase 2, or Omniscope), CMB (Planck + Simons Array (SA) or COrE+), BAO (DESI) and a direct measurement of the Hubble constant on cosmological parameters, paying particular attention to parameters related to the light gravitino, i.e. the fraction of light gravitinos in the total dark matter density $f_{3/2}$, and the effective number of neutrino species for light gravitinos $N_{3/2}$.

When we calculate the Fisher matrices, we choose the following basic set of cosmological parameters: the energy density of matter $\Omega_m h^2$, baryons $\Omega_b h^2$ and the dark energy Ω_Λ, the scalar spectral index n_s, the scalar fluctuation amplitude A_s (the pivot scale is taken to be $k_{\mathrm{pivot}} = 0.05$ Mpc^{-1}), the reionization optical depth τ, and the primordial value of the ^{4}He mass fraction Y_{p}. Fiducial values of these parameters are taken to $(\Omega_m h^2, \Omega_b h^2, \Omega_\Lambda, n_s, A_s \times 10^{10}, \tau, Y_{\mathrm{p}}) = (0.1417, 0.0223, 0.6911, 0.9667, 21.42, 0.066, 0.25)$, which are the best fit values of the Planck result [36]. For the total neutrino mass $\Sigma m_\nu = m_1 + m_2 + m_3$, we fix Σm_ν to a fiducial value $\Sigma m_\nu = 0.06$ eV, or vary it freely. In the following analysis, we fix the neutrino mass hierarchy to be the normal one and the effective number of neutrino species N_ν to be 3.046. For the parameters related to the light gravitino, we set the fiducial value of $N_{3/2}$ to be 0.059 and that of $f_{3/2}$ to be 0.01071 or 0.05353, which corresponds to $m_{3/2} = 1$ eV or 5 eV, respectively when we fix $N_{3/2}$ to be 0.059. For $N_{3/2}$, we fix $N_{3/2} = 0.059$, or treat it as a free parameter.

To obtain Fisher matrices we use CAMB [71, 72][2] for calculations of CMB anisotropies C_l and matter power spectra $P_{\delta\delta}(k)$. In order to combine the CMB experiments with the 21 cm line, BAO and a Hubble H_0 measurement, we calculate the combined Fisher matrix

$$F_{\alpha\beta} = F_{\alpha\beta}^{(21\mathrm{cm})} + F_{\alpha\beta}^{(\mathrm{CMB})} + F_{\alpha\beta}^{(\mathrm{BAO})} + \tilde{F}_{\alpha\beta}^{H_0}. \tag{42}$$

[2] In our analysis of 21 cm line, we neglect non-linear effects for evolutions of the matter power spectrum because we adopt a 21 cm power spectrum only at linear regime. For CMB lensing, by performing a public code HALOFIT [71, 72], we have checked that modifications by including the non-linear effects are much smaller than typical errors in our analyses and have negligible impacts on our constraints.

In this paper, we do not use information for a possible correlation between fluctuations of the 21 cm and the CMB.

4.1 Expected future constraints on light gravitino

In Tables. 6-11, we summarize constraints on cosmological parameters from each combination of experiments.

In Tables 6 and 7, the constraints are for the cases with fixed $N_{3/2} = 0.059$ and $\Sigma m_\nu = 0.06$ eV. With Planck, the Simons Array, DESI (BAO) and a direct measurement of H_0 combined, we obtain a 1 σ error on $f_{3/2}$

$$\sigma(f_{3/2}) = 0.00346, \tag{43}$$

for fiducial $f_{3/2} = 0.01071$, which corresponds to $m_{3/2} = 1$ eV. Adding 21 cm line experiments to them, we see that the constraint on $f_{3/2}$ can be significantly improved. For example, for fiducial $f_{3/2} = 0.01071$, the combination of SKA phase 1 and Planck + Simons Array + DESI + H_0 gives

$$\sigma(f_{3/2}) = 0.00263, \tag{44}$$

while the ones of SKA phase 2 and Planck + Simons Array + DESI + H_0 gives

$$\sigma(f_{3/2}) = 0.00165. \tag{45}$$

We can translate them into errors on the mass of light gravitino $m_{3/2}$. For the case with Planck, the Simons Array, DESI and H_0 combined, the error of $m_{3/2}$ is given as

$$\sigma(m_{3/2}) = 0.33 \text{ eV}. \tag{46}$$

If we add SKA phase 1 or phase 2 to them, the error can be improved as

$$\sigma(m_{3/2}) = 0.25 \text{ eV} \quad \text{(SKA phase 1)}, \tag{47}$$

$$\sigma(m_{3/2}) = 0.16 \text{ eV} \quad \text{(SKA phase 2)}. \tag{48}$$

If we combine Omniscope with Planck + Simons Array + DESI + H_0, the error can improved even further as

$$\sigma(m_{3/2}) = 0.067 \text{ eV} \quad \text{(Omniscope)}. \tag{49}$$

Thus, from these strong improvements, we find that observations of 21 cm line are significantly useful to constrain the mass of light gravitinos.

Next, in Figs. 1-4, we plot contours of 95% confidence levels (C.L.) forecasts of each combination of CMB, 21cm line, BAO and H_0 in $N_{3/2}$-$f_{3/2}$ plane. In the upper panels of Figs. 1-4, we fix the total neutrino mass Σm_ν, and in those of the lower panels, we treat

Σm_ν as a free parameter. In Figs. 1 and 3 the fiducial value of $f_{3/2}$ is set to $f_{3/2} = 0.01071$, which corresponds to $m_{3/2} = 1$ eV when we fix $N_{3/2}$ to be 0.059. In Figs. 2 and 4, the fiducial value of $f_{3/2}$ is set to $f_{3/2} = 0.05353$, which corresponds to $m_{3/2} = 5$ eV when we fix $N_{3/2}$ to be 0.059. In the left two panels of Figs. 1-2, each contour represents constraints from Planck + Simons Array + BAO (DESI) + H_0 measurement or Planck + Simons Array + BAO (DESI) + H_0 measurement + 21cm line (SKA phase 1, phase 2 or Omniscope). In the right two panels of them, each contour represents constraints from COrE+ + BAO (DESI) + H_0 measurement or COrE+ + BAO (DESI) + H_0 measurement + 21cm line (SKA phase 1, phase 2 or Omniscope). In the left two panels of Figs. 3-4, each contour represents constraints by CMB (Planck, Planck + Simons Array or COrE+) only. In the right two panels of them, each contour represents constraints by CMB (Planck, Planck + Simons Array or COrE+) + BAO (DESI) + H_0 measurement.

From Figs. 1-4, we can see that constraints on $N_{3/2}$ and $f_{3/2}$ depend on the fiducial value of $f_{3/2}$. As the fiducial value of $f_{3/2}$ becomes smaller, the constraints on $f_{3/2}$ become better while those on $N_{3/2}$ become worse. The dependences result from the following reasons. From Eq.(4) and (6), the mass of light gravitinos behaves as

$$m_{3/2} \propto f_{3/2} N_{3/2}^{-\frac{3}{4}}. \tag{50}$$

From this equation, we can find that the variation of $m_{3/2}$ due to changing $N_{3/2}$ becomes smaller as the fiducial value of $f_{3/2}$ becomes smaller. Therefore, the influence due to changing $N_{3/2}$ on the growth of perturbations becomes less significant if the fiducial value of $f_{3/2}$ is small. On the other hand, we can see that the constraints on $f_{3/2}$ depend on the fiducial value of $f_{3/2}$ mainly in CMB observation. As the fiducial value of $f_{3/2}$ becomes larger, the free streaming scale of light gravitinos becomes shorter, which makes it more difficult to obtain the information of the gravitino mass from CMB observations because we need to measure higher multi-pole power spectra C_ℓ in order to obtain the information of the free-streaming scales.

Next, from Figs. 3-4, adding the measurement of the Simons Array to the observation of Planck, we see that there are strong improvements on sensitivities to $f_{3/2}$ and $N_{3/2}$ because the Simons Array can precisely observe the CMB polarizations, which is quite useful for getting the information of CMB lensing. COrE+ can further improve the measurement of CMB polarization and hence give tighter constraints. Moreover, adding BAO data to CMB observations, we find that constraints on $N_{3/2}$ are improved somewhat because several parameter degeneracies are broken by those combinations.

From these results, we find that we can detect the nonzero values of $f_{3/2}$ and $N_{3/2}$ at 2σ level by using combinations of next generation CMB observations with BAO data and H_0 if $f_{3/2}$, i.e. $m_{3/2}$ has a relatively large value ($f_{3/2}$ =0.05353, i.e. $m_{3/2} = 5$ eV). However, it is difficult to obtain lower bounds of $N_{3/2}$ even by using COrE+ if $f_{3/2}$ has a relatively small value ($f_{3/2}$ =0.01071, i.e. $m_{3/2} = 1$ eV). Additionally, from the lower panels of Figs.1-4, these constraints becomes weaker when we treat the total neutrino mass as a free parameter because there is a degeneracy between the effect of massive neutrino

and that of light gravitino. In that case, we can obtain a lower bound of $f_{3/2}$ only by using the COrE+ experiment.

On the other hand, from Figs.1-2, adding the 21 cm experiments to the CMB observations, we see that there are substantial improvements. In particular, the combination of SKA phase 1 with Planck + Simons Array, DESI and H_0 has enough sensitivity to obtaining a lower bound of $f_{3/2}$ at 2 σ level even when the fiducial value of $f_{3/2}$ is 0.01071 and we treat the total neutrino mass as a free parameter. Furthermore, the combination of SKA phase 2 with Planck + Simons Array, DESI and H_0 can detect the nonzero value of $N_{3/2}$ except when we treat the total neutrino mass as a free parameter. If we use the combination of SKA phase 2 with COrE+, DESI and H_0, we can detect its nonzero value even in that case. Of course, Omniscope has enough sensitivity to detect the signature of light gravitino in any cases.

Moreover, in Figs. 5, we plot contours of 95% C.L. forecasts of each combination of CMB, 21cm line, DESI and H_0 in Σm_ν-$f_{3/2}$ plane. From the figure, by using the combination of Planck + Simons Array with DESI and H_0, it is difficult to discriminate between effects of massive neutrino and light gravitino if the fiducial value of $f_{3/2}$ is 0.01071. However, even in that case, we can discriminate them and obtain a lower bound of $f_{3/2}$ if we use the combination of SKA phase 1 with Planck + Simons Array, DESI and H_0. Additionally, if we use the combination of SKA phase 2 with COrE+, DESI and H_0 or Omniscope, we can also detect the nonzero neutrino mass, simultaneously.

From our results, we find that 21 cm line observations are quite useful to constrain the mass of light gravitino, and can significantly improve constraints on $f_{3/2}$ and $N_{3/2}$ in combination with CMB, BAO and H_0 observations. Besides, by using 21 cm line observations, we will be able to discriminate between effects of massive neutrino and light gravitino through measuring the difference of their free streaming scales.

5 Conclusion

In this paper, we have studied how well we can constrain the mass of light gravitino $m_{3/2} < \mathcal{O}(10)$ eV, or more specifically, the fraction of light gravitinos in the total dark matter density $f_{3/2}$, and the effective number of neutrino species for light gravitinos $N_{3/2}$, which determine $m_{3/2}$, by using observations of 21 cm line, CMB, BAO and direct measurements of H_0.

In the early Universe, light gravitinos are produced from thermal plasma, and they behave as warm dark matter (WDM) at late epochs. Thus, they imprint characteristic signatures on density fluctuations, and we can detect the features through cosmological observations, such as CMB and 21 cm line. Adding the measurement of the Simons Array, which is a planned precise CMB polarization observation, to the observation of Planck, we see that there are strong improvements on sensitivities to constraints on $f_{3/2}$ and $N_{3/2}$ because the Simons Array is quite useful for getting the information of CMB lensing. If $f_{3/2}$, i.e. $m_{3/2}$ has a relatively large value ($f_{3/2}$ =0.05353, which corresponds

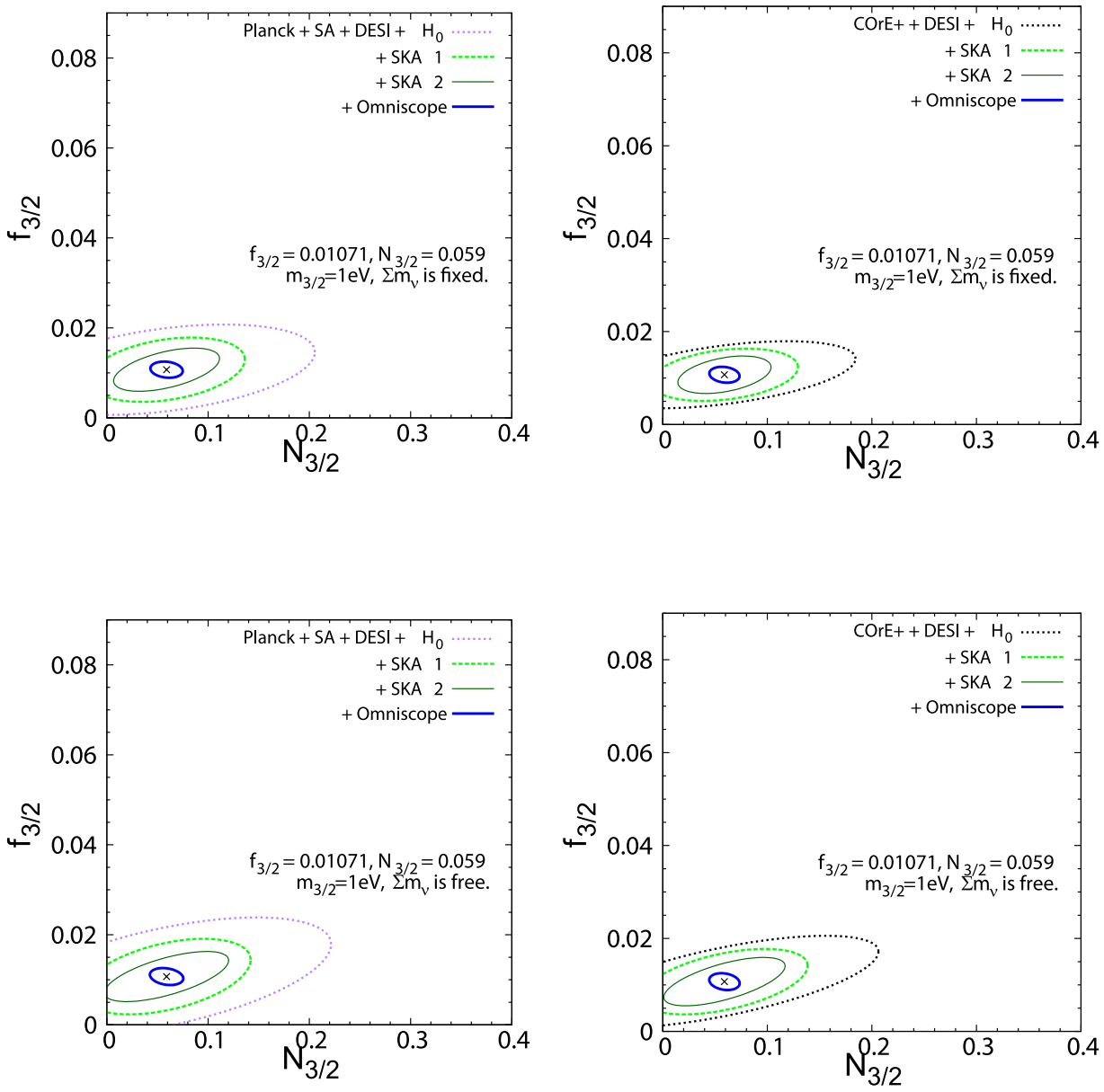


Figure 1: Contours of 95% C.L. forecasts in $N_{3/2}$-$f_{3/2}$ plane. We assume that $f_{3/2} = 0.01071$ and $N_{3/2} = 0.059$, which correspond to $m_{3/2} = 1$ eV. In the upper panels, we fix the total neutrino mass Σm_ν, and in the lower panels, we treat the total neutrino mass as a free parameter. We show constraints from Planck + Simons Array (SA) + DESI (BAO) + H_0 (dotted purple line) with SKA phase 1 (dashed yellow-green line), phase 2 (solid green line) or Omniscope (thick blue line) in the left panels, and COrE+ + DESI (BAO) + H_0 (dotted black line) with SKA phase 1, phase 2 or Omniscope in the right panels.

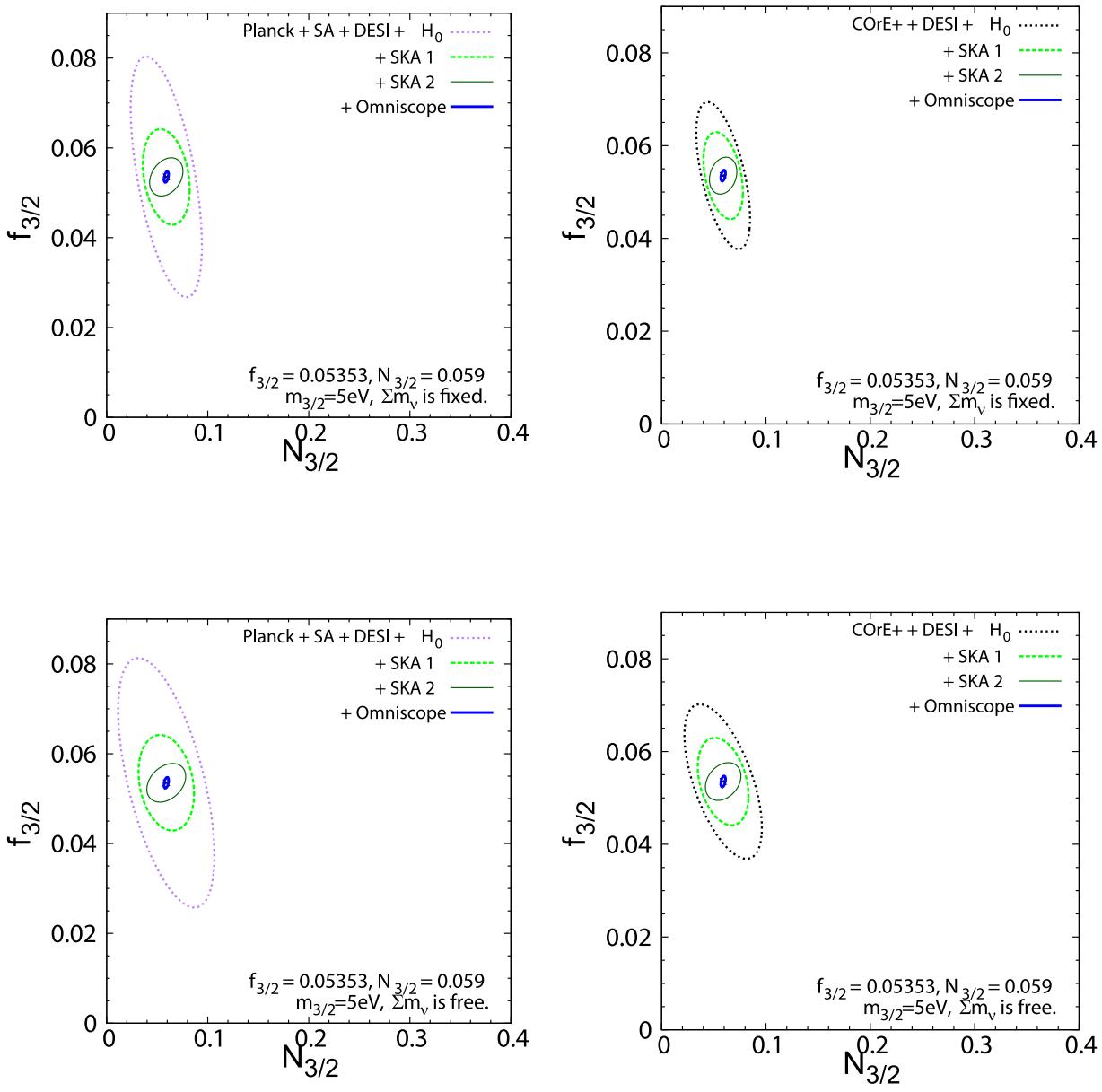


Figure 2: The same as Fig.1 but for $f_{3/2} = 0.05353$ and $N_{3/2} = 0.059$, which correspond to $m_{3/2} = 5$ eV.

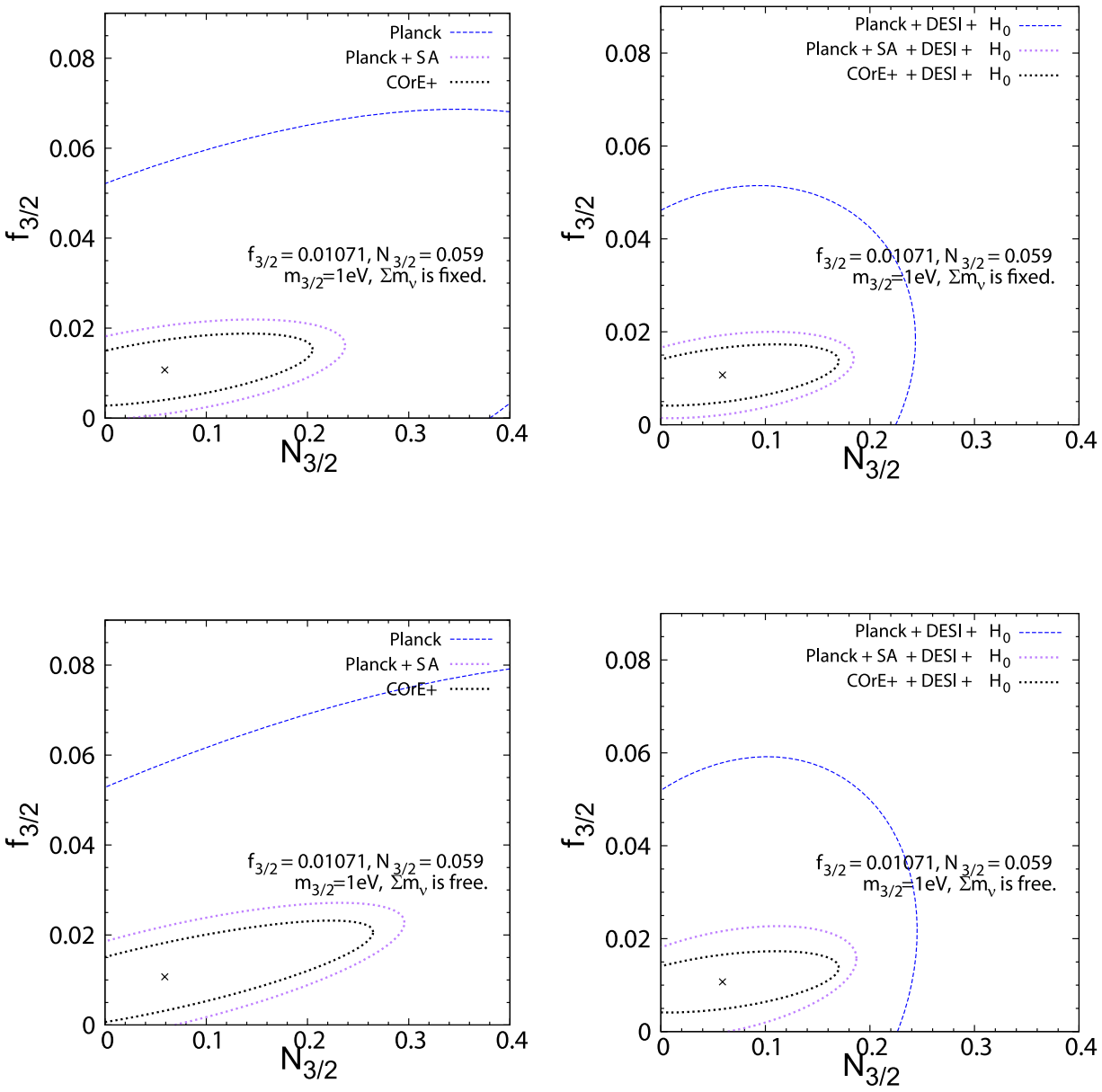


Figure 3: Contours of 95% C.L. forecasts in $N_{3/2}$-$f_{3/2}$ plane by CMB combined with BAO (DESI) and H_0. We assume that $f_{3/2} = 0.01071$ and $N_{3/2} = 0.059$, which correspond to $m_{3/2} = 1$ eV. In the upper panels, we fix the total neutrino mass Σm_ν, and in the lower panels, we treat the total neutrino mass as a free parameter. We show constraints from CMB only (Planck, Planck + Simons Array(SA) and COrE+) in the left panels, and combinations of CMB, BAO (DESI) and H_0 in the right panels.

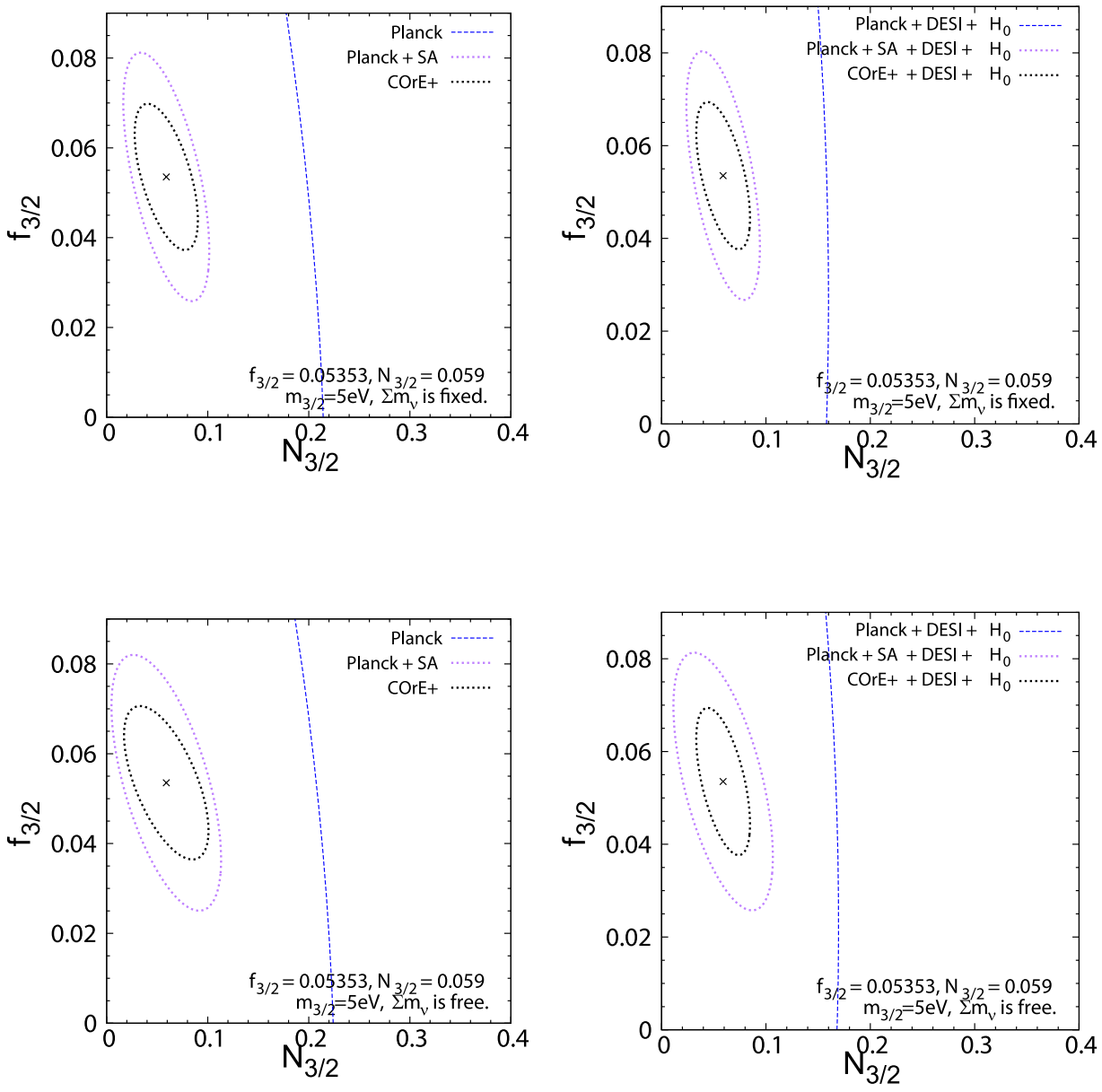


Figure 4: The same as Fig.3 but for $f_{3/2} = 0.05353$ and $N_{3/2} = 0.059$, which correspond to $m_{3/2} = 5$ eV.

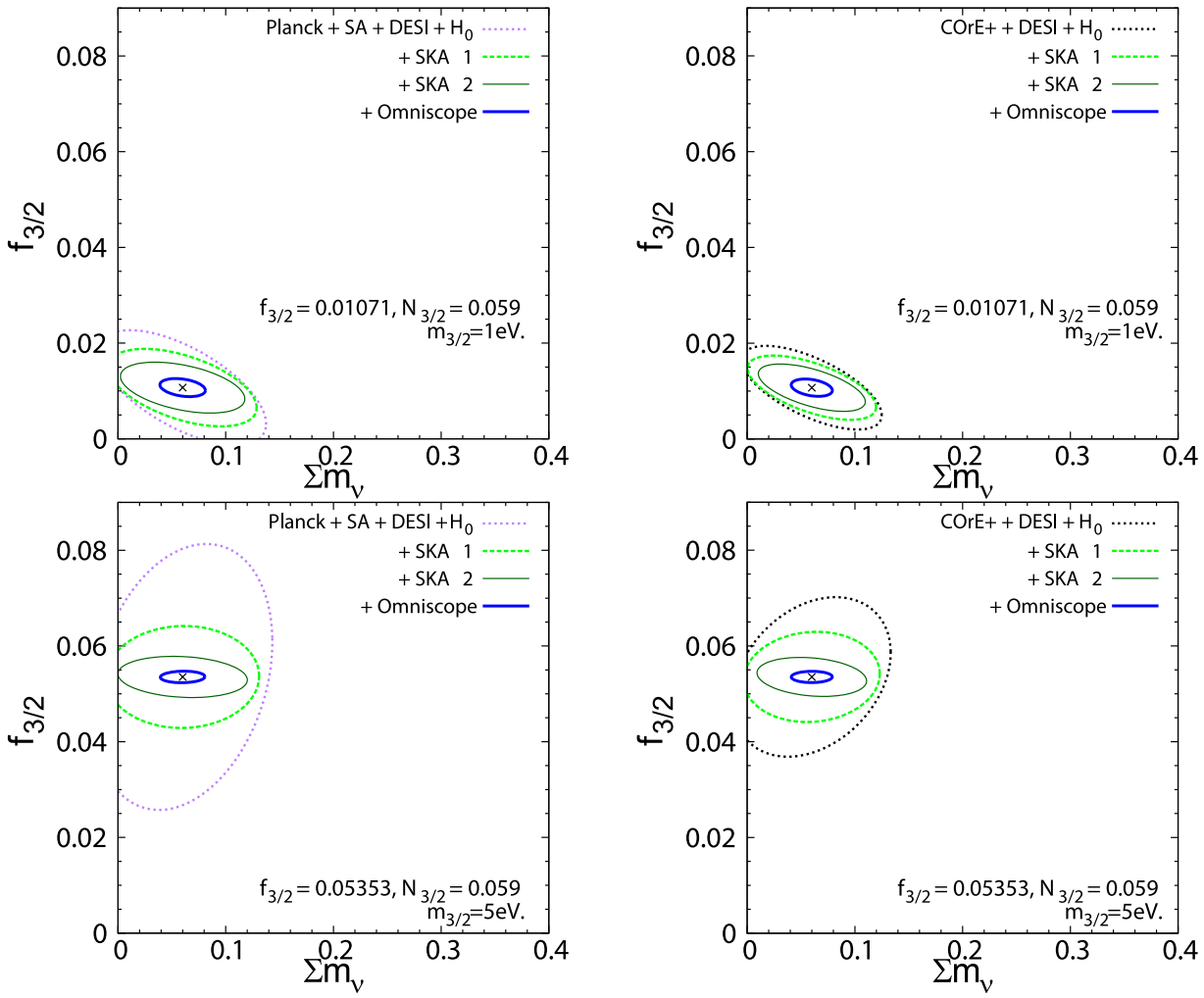


Figure 5: Contours of 95% C.L. forecasts in Σm_ν-$f_{3/2}$ plane. We assume that $\Sigma m_\nu = 0.06$ eV and $N_{3/2} = 0.059$. In the upper panels, we assume $f_{3/2} = 0.01071$, which correspond to $m_{3/2} = 1$ eV and in the lower panels, we assume $f_{3/2} = 0.05353$, which correspond to $m_{3/2} = 5$ eV. We show constraints from Planck + Simons Array (SA) + DESI (BAO) + H_0 (dotted purple line) with SKA phase 1 (dashed yellow-green line), phase 2 (solid green line) or Omniscope (thick blue line) in the left panels, and COrE+ + DESI (BAO) + H_0 (dotted black line) with SKA phase 1, phase 2 or Omniscope in the right panels.

	$\sigma(\Omega_m h^2)$	$\sigma(\Omega_b h^2)$	$\sigma(\Omega_\Lambda)$	$\sigma(n_s)$	$\sigma(A_s \times 10^{10})$
Planck	1.32×10^{-3}	2.07×10^{-4}	9.54×10^{-3}	7.16×10^{-3}	1.92×10^{-1}
+ Simons Array (SA)	5.95×10^{-4}	6.85×10^{-5}	3.87×10^{-3}	2.95×10^{-3}	1.46×10^{-1}
+ SA + BAO + H_0	4.63×10^{-4}	6.28×10^{-5}	2.79×10^{-3}	2.65×10^{-3}	1.42×10^{-1}
+ SA + BAO + H_0 + SKA1	4.17×10^{-4}	6.09×10^{-5}	2.50×10^{-3}	2.57×10^{-3}	1.35×10^{-1}
+ SA + BAO + H_0 + SKA2	3.31×10^{-4}	5.82×10^{-5}	1.88×10^{-3}	2.32×10^{-3}	1.24×10^{-1}
+ SA + BAO + H_0 + Omniscope	6.26×10^{-5}	1.40×10^{-5}	4.68×10^{-4}	1.43×10^{-3}	1.04×10^{-1}
COrE+	4.88×10^{-4}	5.20×10^{-5}	3.08×10^{-3}	2.47×10^{-3}	8.33×10^{-2}
+ BAO + H_0	4.08×10^{-4}	4.97×10^{-5}	2.46×10^{-3}	2.35×10^{-3}	8.27×10^{-2}
+ BAO + H_0 + SKA1	3.70×10^{-4}	4.87×10^{-5}	2.23×10^{-3}	2.28×10^{-3}	8.11×10^{-2}
+ BAO + H_0 + SKA2	2.91×10^{-4}	4.73×10^{-5}	1.66×10^{-3}	2.05×10^{-3}	7.67×10^{-2}
+ BAO + H_0 + Omniscope	6.14×10^{-5}	1.37×10^{-5}	4.57×10^{-4}	1.36×10^{-3}	6.12×10^{-2}
	$\sigma(\tau)$	$\sigma(Y_p)$	$\sigma(f_{3/2})$		
Planck	4.25×10^{-3}	1.13×10^{-2}	1.86×10^{-2}		
+ Simons Array (SA)	3.72×10^{-3}	3.10×10^{-3}	3.95×10^{-3}		
+ SA + BAO + H_0	3.57×10^{-3}	2.96×10^{-3}	3.46×10^{-3}		
+ SA + BAO + H_0 + SKA1	3.41×10^{-3}	2.89×10^{-3}	2.63×10^{-3}		
+ SA + BAO + H_0 + SKA2	3.10×10^{-3}	2.75×10^{-3}	1.65×10^{-3}		
+ SA + BAO + H_0 + Omniscope	2.47×10^{-3}	1.31×10^{-3}	7.13×10^{-4}		
COrE+	2.12×10^{-3}	2.48×10^{-3}	2.69×10^{-3}		
+ BAO + H_0	2.07×10^{-3}	2.43×10^{-3}	2.36×10^{-3}		
+ BAO + H_0 + SKA1	2.04×10^{-3}	2.39×10^{-3}	2.06×10^{-3}		
+ BAO + H_0 + SKA2	1.94×10^{-3}	2.29×10^{-3}	1.47×10^{-3}		
+ BAO + H_0 + Omniscope	1.48×10^{-3}	1.16×10^{-3}	6.78×10^{-4}		

Table 6: 1 σ errors on cosmological parameters for fiducial $f_{3/2} = 0.01071$ ($m_{3/2} = 1$ eV) for the cases with fixed $\Sigma m_\nu = 0.06$ eV and $N_{3/2} = 0.059$.

	$\sigma(\Omega_m h^2)$	$\sigma(\Omega_b h^2)$	$\sigma(\Omega_\Lambda)$	$\sigma(n_s)$	$\sigma(A_s \times 10^{10})$
Planck	1.19×10^{-3}	2.03×10^{-4}	8.08×10^{-3}	6.81×10^{-3}	1.92×10^{-1}
+ Simons Array (SA)	4.57×10^{-4}	6.84×10^{-5}	2.85×10^{-3}	2.86×10^{-3}	1.43×10^{-1}
+ SA + BAO + H_0	4.01×10^{-4}	6.25×10^{-5}	2.33×10^{-3}	2.65×10^{-3}	1.33×10^{-1}
+ SA + BAO + H_0 + SKA1	3.71×10^{-4}	6.06×10^{-5}	2.19×10^{-3}	2.62×10^{-3}	1.30×10^{-1}
+ SA + BAO + H_0 + SKA2	3.07×10^{-4}	5.78×10^{-5}	1.79×10^{-3}	2.51×10^{-3}	1.22×10^{-1}
+ SA + BAO + H_0 + Omniscope	5.22×10^{-5}	1.20×10^{-5}	4.11×10^{-4}	9.73×10^{-4}	1.05×10^{-1}
COrE+	3.25×10^{-4}	5.19×10^{-5}	1.96×10^{-3}	2.43×10^{-3}	8.23×10^{-2}
+ BAO + H_0	3.05×10^{-4}	4.97×10^{-5}	1.77×10^{-3}	2.36×10^{-3}	7.99×10^{-2}
+ BAO + H_0 + SKA1	2.78×10^{-4}	4.87×10^{-5}	1.63×10^{-3}	2.34×10^{-3}	7.87×10^{-2}
+ BAO + H_0 + SKA2	2.42×10^{-4}	4.72×10^{-5}	1.40×10^{-3}	2.28×10^{-3}	7.52×10^{-2}
+ BAO + H_0 + Omniscope	5.10×10^{-5}	1.18×10^{-5}	3.95×10^{-4}	9.56×10^{-4}	6.18×10^{-2}
	$\sigma(\tau)$	$\sigma(Y_p)$	$\sigma(f_{3/2})$		
Planck	4.28×10^{-3}	1.13×10^{-2}	5.73×10^{-2}		
+ Simons Array (SA)	3.71×10^{-3}	3.12×10^{-3}	8.97×10^{-3}		
+ SA + BAO + H_0	3.43×10^{-3}	2.94×10^{-3}	8.88×10^{-3}		
+ SA + BAO + H_0 + SKA1	3.33×10^{-3}	2.85×10^{-3}	4.15×10^{-3}		
+ SA + BAO + H_0 + SKA2	3.08×10^{-3}	2.74×10^{-3}	1.64×10^{-3}		
+ SA + BAO + H_0 + Omniscope	2.50×10^{-3}	1.12×10^{-3}	4.37×10^{-4}		
COrE+	2.13×10^{-3}	2.51×10^{-3}	5.30×10^{-3}		
+ BAO + H_0	2.06×10^{-3}	2.43×10^{-3}	5.22×10^{-3}		
+ BAO + H_0 + SKA1	2.03×10^{-3}	2.37×10^{-3}	3.52×10^{-3}		
+ BAO + H_0 + SKA2	1.93×10^{-3}	2.31×10^{-3}	1.57×10^{-3}		
+ BAO + H_0 + Omniscope	1.47×10^{-3}	9.93×10^{-4}	4.32×10^{-4}		

Table 7: Same as in Table 6 but for fiducial $f_{3/2} = 0.05353$ ($m_{3/2} = 5$ eV).

	$\sigma(\Omega_m h^2)$	$\sigma(\Omega_b h^2)$	$\sigma(\Omega_\Lambda)$	$\sigma(n_s)$	$\sigma(A_s \times 10^{10})$
Planck	5.44×10^{-3}	2.12×10^{-4}	2.04×10^{-2}	7.37×10^{-3}	2.06×10^{-1}
+ Simons Array (SA)	2.06×10^{-3}	6.86×10^{-5}	7.14×10^{-3}	2.97×10^{-3}	1.71×10^{-1}
+ SA + BAO + H_0	1.42×10^{-3}	6.32×10^{-5}	4.93×10^{-3}	2.65×10^{-3}	1.57×10^{-1}
+ SA + BAO + H_0 + SKA1	8.16×10^{-4}	6.22×10^{-5}	3.21×10^{-3}	2.57×10^{-3}	1.46×10^{-1}
+ SA + BAO + H_0 + SKA2	5.16×10^{-4}	5.95×10^{-5}	2.13×10^{-3}	2.32×10^{-3}	1.39×10^{-1}
+ SA + BAO + H_0 + Omniscope	6.26×10^{-5}	2.27×10^{-5}	4.92×10^{-4}	1.58×10^{-3}	1.06×10^{-1}
COrE+	1.77×10^{-3}	5.21×10^{-5}	6.19×10^{-3}	2.47×10^{-3}	1.00×10^{-1}
+ BAO + H_0	1.31×10^{-3}	4.98×10^{-5}	4.58×10^{-3}	2.35×10^{-3}	9.32×10^{-2}
+ BAO + H_0 + SKA1	7.93×10^{-4}	4.94×10^{-5}	3.06×10^{-3}	2.29×10^{-3}	8.70×10^{-2}
+ BAO + H_0 + SKA2	5.05×10^{-4}	4.81×10^{-5}	2.06×10^{-3}	2.08×10^{-3}	8.44×10^{-2}
+ BAO + H_0 + Omniscope	6.14×10^{-5}	2.11×10^{-5}	4.81×10^{-4}	1.50×10^{-3}	6.42×10^{-2}
	$\sigma(\tau)$	$\sigma(Y_p)$	$\sigma(f_{3/2})$	$\sigma(N_{3/2})$	
Planck	4.27×10^{-3}	1.59×10^{-2}	2.34×10^{-2}	1.93×10^{-1}	
+ Simons Array (SA)	3.83×10^{-3}	4.43×10^{-3}	4.52×10^{-3}	7.19×10^{-2}	
+ SA + BAO + H_0	3.65×10^{-3}	3.83×10^{-3}	3.75×10^{-3}	5.07×10^{-2}	
+ SA + BAO + H_0 + SKA1	3.55×10^{-3}	3.42×10^{-3}	2.79×10^{-3}	2.98×10^{-2}	
+ SA + BAO + H_0 + SKA2	3.39×10^{-3}	3.17×10^{-3}	1.92×10^{-3}	2.07×10^{-2}	
+ SA + BAO + H_0 + Omniscope	2.57×10^{-3}	2.06×10^{-3}	7.23×10^{-4}	6.43×10^{-3}	
COrE+	2.13×10^{-3}	3.63×10^{-3}	3.26×10^{-3}	5.89×10^{-2}	
+ BAO + H_0	2.08×10^{-3}	3.22×10^{-3}	2.66×10^{-3}	4.48×10^{-2}	
+ BAO + H_0 + SKA1	2.07×10^{-3}	2.86×10^{-3}	2.16×10^{-3}	2.73×10^{-2}	
+ BAO + H_0 + SKA2	2.03×10^{-3}	2.65×10^{-3}	1.61×10^{-3}	1.77×10^{-2}	
+ BAO + H_0 + Omniscope	1.58×10^{-3}	1.80×10^{-3}	6.88×10^{-4}	5.80×10^{-3}	

Table 8: 1 σ errors on cosmological parameters for fiducial $f_{3/2} = 0.01071$ and $N_{3/2} = 0.059$ ($m_{3/2} = 1$ eV) for the cases with fixed $\Sigma m_\nu = 0.06$ eV.

	$\sigma(\Omega_m h^2)$	$\sigma(\Omega_b h^2)$	$\sigma(\Omega_\Lambda)$	$\sigma(n_s)$	$\sigma(A_s \times 10^{10})$
Planck	2.98×10^{-3}	2.09×10^{-4}	1.40×10^{-2}	7.19×10^{-3}	1.97×10^{-1}
+ Simons Array (SA)	1.02×10^{-3}	6.90×10^{-5}	5.26×10^{-3}	3.07×10^{-3}	1.53×10^{-1}
+ SA + BAO + H_0	7.48×10^{-4}	6.27×10^{-5}	3.64×10^{-3}	2.68×10^{-3}	1.51×10^{-1}
+ SA + BAO + H_0 + SKA1	5.48×10^{-4}	6.06×10^{-5}	2.88×10^{-3}	2.64×10^{-3}	1.42×10^{-1}
+ SA + BAO + H_0 + SKA2	3.95×10^{-4}	5.79×10^{-5}	2.14×10^{-3}	2.52×10^{-3}	1.33×10^{-1}
+ SA + BAO + H_0 + Omniscope	5.38×10^{-5}	1.48×10^{-5}	4.28×10^{-4}	1.07×10^{-3}	1.06×10^{-1}
COrE+	8.56×10^{-4}	5.26×10^{-5}	4.44×10^{-3}	2.67×10^{-3}	8.72×10^{-2}
+ BAO + H_0	6.63×10^{-4}	4.97×10^{-5}	3.32×10^{-3}	2.43×10^{-3}	8.70×10^{-2}
+ BAO + H_0 + SKA1	5.23×10^{-4}	4.88×10^{-5}	2.72×10^{-3}	2.38×10^{-3}	8.46×10^{-2}
+ BAO + H_0 + SKA2	3.81×10^{-4}	4.74×10^{-5}	2.04×10^{-3}	2.30×10^{-3}	8.18×10^{-2}
+ BAO + H_0 + Omniscope	5.29×10^{-5}	1.45×10^{-5}	4.15×10^{-4}	1.04×10^{-3}	6.22×10^{-2}
	$\sigma(\tau)$	$\sigma(Y_p)$	$\sigma(f_{3/2})$	$\sigma(N_{3/2})$	
Planck	4.29×10^{-3}	1.14×10^{-2}	6.47×10^{-2}	6.33×10^{-2}	
+ Simons Array (SA)	3.79×10^{-3}	3.29×10^{-3}	1.12×10^{-2}	1.71×10^{-2}	
+ SA + BAO + H_0	3.70×10^{-3}	2.97×10^{-3}	1.08×10^{-2}	1.42×10^{-2}	
+ SA + BAO + H_0 + SKA1	3.54×10^{-3}	2.87×10^{-3}	4.29×10^{-3}	9.33×10^{-3}	
+ SA + BAO + H_0 + SKA2	3.29×10^{-3}	2.76×10^{-3}	1.72×10^{-3}	6.65×10^{-3}	
+ SA + BAO + H_0 + Omniscope	2.52×10^{-3}	1.12×10^{-3}	4.83×10^{-4}	9.10×10^{-4}	
COrE+	2.14×10^{-3}	2.62×10^{-3}	6.57×10^{-3}	1.26×10^{-2}	
+ BAO + H_0	2.10×10^{-3}	2.45×10^{-3}	6.40×10^{-3}	1.04×10^{-2}	
+ BAO + H_0 + SKA1	2.08×10^{-3}	2.39×10^{-3}	3.79×10^{-3}	7.62×10^{-3}	
+ BAO + H_0 + SKA2	2.01×10^{-3}	2.32×10^{-3}	1.60×10^{-3}	5.29×10^{-3}	
+ BAO + H_0 + Omniscope	1.50×10^{-3}	9.93×10^{-4}	4.73×10^{-4}	8.93×10^{-4}	

Table 9: Same as in Table 8 but for fiducial $f_{3/2} = 0.05353$ ($m_{3/2} = 5$ eV).

	$\sigma(\Omega_m h^2)$	$\sigma(\Omega_b h^2)$	$\sigma(\Omega_\Lambda)$	$\sigma(n_s)$	$\sigma(A_s \times 10^{10})$
Planck	5.51×10^{-3}	2.35×10^{-4}	2.47×10^{-2}	7.61×10^{-3}	2.07×10^{-1}
+ Simons Array (SA)	2.09×10^{-3}	7.27×10^{-5}	9.53×10^{-3}	3.39×10^{-3}	1.77×10^{-1}
+ SA + BAO + H_0	1.43×10^{-3}	6.50×10^{-5}	5.05×10^{-3}	2.72×10^{-3}	1.68×10^{-1}
+ SA + BAO + H_0 + SKA1	8.18×10^{-4}	6.43×10^{-5}	3.61×10^{-3}	2.60×10^{-3}	1.63×10^{-1}
+ SA + BAO + H_0 + SKA2	5.19×10^{-4}	6.31×10^{-5}	2.37×10^{-3}	2.34×10^{-3}	1.58×10^{-1}
+ SA + BAO + H_0 + Omniscope	7.78×10^{-5}	2.29×10^{-5}	6.65×10^{-4}	1.60×10^{-3}	1.16×10^{-1}
COrE+	1.80×10^{-3}	5.50×10^{-5}	8.27×10^{-3}	3.03×10^{-3}	1.00×10^{-1}
+ BAO + H_0	1.32×10^{-3}	5.04×10^{-5}	4.72×10^{-3}	2.35×10^{-3}	9.50×10^{-2}
+ BAO + H_0 + SKA1	7.94×10^{-4}	5.00×10^{-5}	3.51×10^{-3}	2.29×10^{-3}	9.08×10^{-2}
+ BAO + H_0 + SKA2	5.10×10^{-4}	4.94×10^{-5}	2.34×10^{-3}	2.08×10^{-3}	8.87×10^{-2}
+ BAO + H_0 + Omniscope	7.46×10^{-5}	2.15×10^{-5}	6.50×10^{-4}	1.51×10^{-3}	7.30×10^{-2}
	$\sigma(\tau)$	$\sigma(Y_p)$	$\sigma(f_{3/2})$	$\sigma(N_{3/2})$	$\sigma(\Sigma m_\nu)$
Planck	4.29×10^{-3}	1.66×10^{-2}	2.82×10^{-2}	2.38×10^{-1}	2.02×10^{-1}
+ Simons Array (SA)	4.07×10^{-3}	4.85×10^{-3}	6.63×10^{-3}	9.55×10^{-2}	8.44×10^{-2}
+ SA + BAO + H_0	3.97×10^{-3}	3.95×10^{-3}	4.84×10^{-3}	5.17×10^{-2}	3.13×10^{-2}
+ SA + BAO + H_0 + SKA1	3.95×10^{-3}	3.52×10^{-3}	3.26×10^{-3}	3.04×10^{-2}	2.77×10^{-2}
+ SA + BAO + H_0 + SKA2	3.87×10^{-3}	3.35×10^{-3}	2.14×10^{-3}	2.26×10^{-2}	2.33×10^{-2}
+ SA + BAO + H_0 + Omniscope	2.76×10^{-3}	2.07×10^{-3}	7.60×10^{-4}	6.65×10^{-3}	8.51×10^{-3}
COrE+	2.16×10^{-3}	4.11×10^{-3}	5.04×10^{-3}	8.30×10^{-2}	7.04×10^{-2}
+ BAO + H_0	2.15×10^{-3}	3.33×10^{-3}	3.52×10^{-3}	4.71×10^{-2}	2.62×10^{-2}
+ BAO + H_0 + SKA1	2.15×10^{-3}	2.92×10^{-3}	2.71×10^{-3}	2.86×10^{-2}	2.41×10^{-2}
+ BAO + H_0 + SKA2	2.13×10^{-3}	2.78×10^{-3}	1.99×10^{-3}	2.11×10^{-2}	2.00×10^{-2}
+ BAO + H_0 + Omniscope	1.73×10^{-3}	1.80×10^{-3}	7.29×10^{-4}	5.86×10^{-3}	7.69×10^{-3}

Table 10: 1 σ errors on cosmological parameters for fiducial $f_{3/2} = 0.01071$ and $N_{3/2} = 0.059$ ($m_{3/2} = 1$ eV) for the cases with freely varying Σm_ν.

	$\sigma(\Omega_m h^2)$	$\sigma(\Omega_b h^2)$	$\sigma(\Omega_\Lambda)$	$\sigma(n_s)$	$\sigma(A_s \times 10^{10})$
Planck	3.45×10^{-3}	2.43×10^{-4}	2.48×10^{-2}	7.58×10^{-3}	1.97×10^{-1}
+ Simons Array (SA)	1.23×10^{-3}	7.19×10^{-5}	9.65×10^{-3}	3.17×10^{-3}	1.72×10^{-1}
+ SA + BAO + H_0	7.74×10^{-4}	6.48×10^{-5}	3.71×10^{-3}	2.83×10^{-3}	1.60×10^{-1}
+ SA + BAO + H_0 + SKA1	5.52×10^{-4}	6.33×10^{-5}	3.29×10^{-3}	2.72×10^{-3}	1.59×10^{-1}
+ SA + BAO + H_0 + SKA2	3.96×10^{-4}	6.19×10^{-5}	2.41×10^{-3}	2.66×10^{-3}	1.56×10^{-1}
+ SA + BAO + H_0 + Omniscope	7.60×10^{-5}	1.61×10^{-5}	6.84×10^{-4}	1.13×10^{-3}	1.13×10^{-1}
COrE+	1.08×10^{-3}	5.42×10^{-5}	8.46×10^{-3}	2.81×10^{-3}	9.37×10^{-2}
+ BAO + H_0	6.70×10^{-4}	5.05×10^{-5}	3.51×10^{-3}	2.48×10^{-3}	8.89×10^{-2}
+ BAO + H_0 + SKA1	5.30×10^{-4}	4.97×10^{-5}	3.24×10^{-3}	2.40×10^{-3}	8.84×10^{-2}
+ BAO + H_0 + SKA2	3.85×10^{-4}	4.88×10^{-5}	2.37×10^{-3}	2.34×10^{-3}	8.76×10^{-2}
+ BAO + H_0 + Omniscope	7.37×10^{-5}	1.56×10^{-5}	6.64×10^{-4}	1.08×10^{-3}	6.95×10^{-2}
	$\sigma(\tau)$	$\sigma(Y_p)$	$\sigma(f_{3/2})$	$\sigma(N_{3/2})$	$\sigma(\Sigma m_\nu)$
Planck	4.29×10^{-3}	1.16×10^{-2}	6.48×10^{-2}	6.72×10^{-2}	1.73×10^{-1}
+ Simons Array (SA)	4.07×10^{-3}	3.29×10^{-3}	1.15×10^{-2}	2.19×10^{-2}	7.40×10^{-2}
+ SA + BAO + H_0	3.96×10^{-3}	3.24×10^{-3}	1.12×10^{-2}	1.92×10^{-2}	3.36×10^{-2}
+ SA + BAO + H_0 + SKA1	3.91×10^{-3}	3.05×10^{-3}	4.29×10^{-3}	1.11×10^{-2}	2.86×10^{-2}
+ SA + BAO + H_0 + SKA2	3.85×10^{-3}	2.97×10^{-3}	1.73×10^{-3}	7.75×10^{-3}	2.42×10^{-2}
+ SA + BAO + H_0 + Omniscope	2.66×10^{-3}	1.25×10^{-3}	4.84×10^{-4}	9.30×10^{-4}	8.33×10^{-3}
COrE+	2.16×10^{-3}	2.63×10^{-3}	6.89×10^{-3}	1.69×10^{-2}	6.15×10^{-2}
+ BAO + H_0	2.16×10^{-3}	2.61×10^{-3}	6.72×10^{-3}	1.50×10^{-2}	2.96×10^{-2}
+ BAO + H_0 + SKA1	2.15×10^{-3}	2.49×10^{-3}	3.80×10^{-3}	9.80×10^{-3}	2.54×10^{-2}
+ BAO + H_0 + SKA2	2.13×10^{-3}	2.43×10^{-3}	1.64×10^{-3}	6.86×10^{-3}	2.05×10^{-2}
+ BAO + H_0 + Omniscope	1.64×10^{-3}	1.09×10^{-3}	4.73×10^{-4}	9.19×10^{-4}	7.66×10^{-3}

Table 11: Same as in Table 10 but for fiducial $f_{3/2} = 0.05353$ ($m_{3/2} = 5$ eV).

to $m_{3/2} = 5$ eV), by using Planck + Simons Array or COrE+, we can detect the nonzero values of $f_{3/2}$ and $N_{3/2}$ at 2σ level.

Besides, adding the 21 cm experiments to the CMB observations, we see that there are substantial improvements. For the cases with fixed $N_{3/2} = 0.059$ and $\Sigma m_\nu = 0.06$ eV, by combining SKA phase 1 with Planck, the Simons Array, DESI and a direct measurement of H_0 at 1% accuracy, we can obtain a 1 σ error on the mass of light gravitinos, $\sigma(m_{3/2}) = 0.25$ eV for fiducial $f_{3/2} = 0.01071$, which corresponds to $m_{3/2} = 1$ eV. If we use SKA phase 2 or Omniscope, the error can be improved as $\sigma(m_{3/2}) = 0.16$ eV (SKA phase 2) or $\sigma(m_{3/2}) = 0.067$ eV (Omniscope), respectively. In particular, the combination of SKA phase 1 with Planck + Simons Array, DESI and H_0 has enough sensitivity to obtaining a lower bound of $f_{3/2}$ at 2 σ level even when the fiducial value of $f_{3/2}$ is as small as 0.01071 and we treat $N_{3/2}$ and the total neutrino mass as free parameters. Furthermore, the combination of SKA phase 2 with Planck + Simons Array, DESI and H_0 can detect the nonzero value of $N_{3/2}$ except when we treat the total neutrino mass as a free parameter. Moreover, if we use the combination of SKA phase 2 with COrE+, DESI and H_0, we can detect the nonzero value of $N_{3/2}$ even in that case.

Although it is difficult to discriminate between the effects of massive neutrinos and light gravitinos only by using Planck + Simons Array, BAO and a measurement of H_0, it becomes feasible if a precise observation of 21 cm line is incorporated. In particular, the combination of SKA phase 2 with COrE+, DESI and H_0 has enough sensitivities to determine the parameters of light gravitino and the total neutrino mass at 2 σ level, simultaneously. If we use Omniscope, we can detect features of light gravitinos and massive neutrinos even with on-going CMB observations.

Our results indicate that combining 21 cm line observations with CMB observations has strong impacts on the determination of the mass of light gravitinos and understanding the origin of matter in the Universe.

Acknowledgments

We thank Tomo Takahashi for a useful correspondence about cosmological effects of light gravitino. Besides, we appreciate the significant contribution made by Toyokazu Sekiguchi. This work is supported by MEXT KAKENHI Grant Number 15H05889 (M. K.), JSPS KAKENHI Grant Number 25400248 (M. K.) and also by the World Premier International Research Center Initiative (WPI), MEXT, Japan.

References

[1] T. Moroi, H. Murayama and M. Yamaguchi, Phys. Lett. B **303**, 289 (1993). doi:10.1016/0370-2693(93)91434-O

[2] M. Fukugita and T. Yanagida, Phys. Lett. B **174**, 45 (1986). doi:10.1016/0370-2693(86)91126-3

[3] K. Hamaguchi, S. Shirai and T. T. Yanagida, Phys. Lett. B **651**, 44 (2007) doi:10.1016/j.physletb.2007.05.063 [arXiv:0705.0219 [hep-ph]].

[4] E. Pierpaoli, S. Borgani, A. Masiero and M. Yamaguchi, Phys. Rev. D **57**, 2089 (1998) doi:10.1103/PhysRevD.57.2089 [astro-ph/9709047].

[5] M. Viel, J. Lesgourgues, M. G. Haehnelt, S. Matarrese and A. Riotto, Phys. Rev. D **71**, 063534 (2005) doi:10.1103/PhysRevD.71.063534 [astro-ph/0501562].

[6] K. Ichikawa, M. Kawasaki, K. Nakayama, T. Sekiguchi and T. Takahashi, JCAP **0908**, 013 (2009) doi:10.1088/1475-7516/2009/08/013 [arXiv:0905.2237 [astro-ph.CO]].

[7] A. Kamada, M. Shirasaki and N. Yoshida, JHEP **1406**, 162 (2014) doi:10.1007/JHEP06(2014)162 [arXiv:1311.4323 [hep-ph]].

[8] K. Osato, T. Sekiguchi, M. Shirasaki, A. Kamada and N. Yoshida, arXiv:1601.07386 [astro-ph.CO].

[9] M. McQuinn, O. Zahn, M. Zaldarriaga, L. Hernquist and S. R. Furlanetto, Astrophys. J. **653**, 815 (2006) [arXiv:astro-ph/0512263].

[10] A. Loeb and S. Wyithe, Phys. Rev. Lett. **100**, 161301 (2008).

[11] J. R. Pritchard and E. Pierpaoli, Phys. Rev. D **78**, 065009 (2008).

[12] J. R. Pritchard and E. Pierpaoli, Nucl. Phys. Proc. Suppl. **188**, 31 (2009).

[13] K. N. Abazajian, E. Calabrese, A. Cooray, F. De Bernardis, S. Dodelson, A. Friedland, G. M. Fuller and S. Hannestad *et al.*, Astropart. Phys. **35**, 177 (2011) [arXiv:1103.5083 [astro-ph.CO]].

[14] Y. Oyama, A. Shimizu and K. Kohri, Phys. Lett. B **718**, 1186 (2013) [arXiv:1205.5223 [astro-ph.CO]].

[15] K. Kohri, Y. Oyama, T. Sekiguchi and T. Takahashi, JCAP **1310**, 065 (2013) [arXiv:1303.1688 [astro-ph.CO]].

[16] K. Kohri, Y. Oyama, T. Sekiguchi and T. Takahashi, JCAP **1409**, 014 (2014) [arXiv:1404.4847 [astro-ph.CO]].

[17] Y. Oyama, "Constraints on the neutrino parameters by future cosmological 21cm line and precise CMB polarization observations (PhD thesis, The Graduate University for Advanced Studies (SOKENDAI))," arXiv:1510.05161 [astro-ph.CO].

[18] Y. Oyama, K. Kohri and M. Hazumi, JCAP **1602**, no. 02, 008 (2016) [arXiv:1510.03806 [astro-ph.CO]].

[19] http://www.skatelescope.org/

[20] M. Tegmark and M. Zaldarriaga, Phys. Rev. D **79**, 083530 (2009) [arXiv:0805.4414 [astro-ph]].

[21] M. Tegmark and M. Zaldarriaga, Phys. Rev. D **82**, 103501 (2010) [arXiv:0909.0001 [astro-ph.CO]].

[22] https://www.simonsfoundation.org/

[23] http://www.core-mission.org

[24] http://desi.lbl.gov/

[25] M. Dine and W. Fischler, Phys. Lett. B **110**, 227 (1982). doi:10.1016/0370-2693(82)91241-2

[26] C. R. Nappi and B. A. Ovrut, Phys. Lett. B **113**, 175 (1982). doi:10.1016/0370-2693(82)90418-X

[27] L. Alvarez-Gaume, M. Claudson and M. B. Wise, Nucl. Phys. B **207**, 96 (1982). doi:10.1016/0550-3213(82)90138-9

[28] M. Dine and A. E. Nelson, Phys. Rev. D **48**, 1277 (1993) doi:10.1103/PhysRevD.48.1277 [hep-ph/9303230].

[29] M. Dine, A. E. Nelson and Y. Shirman, Phys. Rev. D **51**, 1362 (1995) doi:10.1103/PhysRevD.51.1362 [hep-ph/9408384].

[30] M. Dine, A. E. Nelson, Y. Nir and Y. Shirman, Phys. Rev. D **53**, 2658 (1996) doi:10.1103/PhysRevD.53.2658 [hep-ph/9507378].

[31] G. Aad *et al.* [ATLAS and CMS Collaborations], Phys. Rev. Lett. **114**, 191803 (2015) doi:10.1103/PhysRevLett.114.191803 [arXiv:1503.07589 [hep-ex]].

[32] S. Chatrchyan *et al.* [CMS Collaboration], Phys. Lett. B **716**, 30 (2012) doi:10.1016/j.physletb.2012.08.021 [arXiv:1207.7235 [hep-ex]].

[33] M. A. Ajaib, I. Gogoladze, F. Nasir and Q. Shafi, Phys. Lett. B **713**, 462 (2012) doi:10.1016/j.physletb.2012.06.036 [arXiv:1204.2856 [hep-ph]].

[34] T. T. Yanagida, N. Yokozaki and K. Yonekura, JHEP **1210**, 017 (2012) doi:10.1007/JHEP10(2012)017 [arXiv:1206.6589 [hep-ph]].

[35] G. Aad *et al.* [ATLAS Collaboration], JHEP **1409**, 103 (2014) doi:10.1007/JHEP09(2014)103 [arXiv:1407.0603 [hep-ex]].

[36] P. A. R. Ade *et al.* [Planck Collaboration], arXiv:1502.01589 [astro-ph.CO].

[37] K. Hamaguchi, S. Shirai and T. T. Yanagida, Phys. Lett. B **654**, 110 (2007) doi:10.1016/j.physletb.2007.08.047 [arXiv:0707.2463 [hep-ph]].

[38] S. Furlanetto, S. P. Oh and F. Briggs, Phys. Rept. **433**, 181 (2006).

[39] J. R. Pritchard and A. Loeb, arXiv:1109.6012 [astro-ph.CO].

[40] P. Madau, A. Meiksin and M. J. Rees, Astrophys. J. **475**, 429 (1997) [arXiv:astro-ph/9608010].

[41] S. Furlanetto, Mon. Not. Roy. Astron. Soc. **371**, 867 (2006) [arXiv:astro-ph/0604040].

[42] J. R. Pritchard and A. Loeb, Phys. Rev. D **78**, 103511 (2008) [arXiv:0802.2102 [astro-ph]].

[43] S. A. Wouthuysen, Astron. J. **57**, 31 (1952).

[44] G. B. Field, Proc. IRE. **46**, 240 (1958).

[45] Y. Mao, M. Tegmark, M. McQuinn, M. Zaldarriaga and O. Zahn, Phys. Rev. D **78**, 023529 (2008) [arXiv:0802.1710 [astro-ph]].

[46] M. McQuinn, A. Lidz, O. Zahn, S. Dutta, L. Hernquist and M. Zaldarriaga, Mon. Not. Roy. Astron. Soc. **377**, 1043 (2007) [astro-ph/0610094].

[47] M. McQuinn, L. Hernquist, M. Zaldarriaga and S. Dutta, Mon. Not. Roy. Astron. Soc. **381**, 75 (2007) [arXiv:0704.2239 [astro-ph]].

[48] M. Tegmark, A. Taylor and A. Heavens, Astrophys. J. **480**, 22 (1997) [arXiv:astro-ph/9603021].

[49] E. Chapman, F. B. Abdalla, G. Harker, V. Jelic, P. Labropoulos, S. Zaroubi, M. A. Brentjens and A. G. de Bruyn *et al.*, arXiv:1201.2190 [astro-ph.CO].

[50] http://www.lofar.org/

[51] G. Mellema, L. V. E. Koopmans, F. A. Abdalla, G. Bernardi, B. Ciardi, S. Daiboo, A. G. de Bruyn and K. K. Datta *et al.*, Exper. Astron. **36**, 235 (2013) [arXiv:1210.0197 [astro-ph.CO]].

[52] J. Lesgourgues and S. Pastor, Phys. Rept. **429**, 307 (2006) [arXiv:astro-ph/0603494].

[53] Y. Y. Y. Wong, Ann. Rev. Nucl. Part. Sci. **61**, 69 (2011) [arXiv:1111.1436 [astro-ph.CO]].

[54] J. Lesgourgues, S. Pastor and L. Perotto, Phys. Rev. D **70**, 045016 (2004) [hep-ph/0403296].

[55] M. Takada, E. Komatsu and T. Futamase, Phys. Rev. D **73**, 083520 (2006) [astro-ph/0512374].

[56] A. Slosar, Phys. Rev. D **73**, 123501 (2006) [astro-ph/0602133].

[57] F. De Bernardis, T. D. Kitching, A. Heavens and A. Melchiorri, Phys. Rev. D **80**, 123509 (2009) [arXiv:0907.1917 [astro-ph.CO]].

[58] R. Jimenez, T. Kitching, C. Pena-Garay and L. Verde, JCAP **1005**, 035 (2010) [arXiv:1003.5918 [astro-ph.CO]].

[59] T. Okamoto and W. Hu, Phys. Rev. D **67**, 083002 (2003)[astro-ph/0301031].

[60] http://lpsc.in2p3.fr/perotto/

[61] D. Baumann *et al.* [CMBPol Study Team Collaboration], AIP Conf. Proc. **1141**, 10 (2009) [arXiv:0811.3919 [astro-ph]].

[62] L. Verde, H. Peiris and R. Jimenez, JCAP **0601**, 019 (2006) [astro-ph/0506036].

[63] N. Katayama and E. Komatsu, Astrophys. J. **737**, 78 (2011) [arXiv:1101.5210 [astro-ph.CO]].

[64] L. Page *et al.* [WMAP Collaboration], Astrophys. J. Suppl. **170**, 335 (2007) [astro-ph/0603450].

[65] E. M. Leitch, J. M. Kovac, N. W. Halverson, J. E. Carlstrom, C. Pryke and M. W. E. Smith, Astrophys. J. **624**, 10 (2005) [astro-ph/0409357].

[66] D. P. Finkbeiner, M. Davis and D. J. Schlegel, Astrophys. J. **524**, 867 (1999) [astro-ph/9905128].

[67] J. Tauber *et al.* [Planck Collaboration], astro-ph/0604069.

[68] A. Albrecht, G. Bernstein, R. Cahn, W. L. Freedman, J. Hewitt, W. Hu, J. Huth and M. Kamionkowski *et al.*, astro-ph/0609591.

[69] W. L. K. Wu, J. Errard, C. Dvorkin, C. L. Kuo, A. T. Lee, P. McDonald, A. Slosar and O. Zahn, Astrophys. J. **788**, 138 (2014) [arXiv:1402.4108 [astro-ph.CO]].

[70] A. Font-Ribera, P. McDonald, N. Mostek, B. A. Reid, H. J. Seo and A. Slosar, JCAP **1405**, 023 (2014) [arXiv:1308.4164 [astro-ph.CO]].

[71] A. Lewis, A. Challinor and A. Lasenby, Astrophys. J. **538**, 473 (2000) [astro-ph/9911177].

[72] http://camb.info/